MASTERARBEIT | MASTER'S THESIS

Titel | Title

Fluorinated hypercrosslinked polymers for the adsorption of organic pollutants from wastewater

verfasst von | submitted by

Le Tang BSc

angestrebter akademischer Grad | in partial fulfilment of the requirements for the degree of

Master of Science (MSc)

Wien | Vienna, 2024

Studienkennzahl lt. Studienblatt | Degree programme code as it appears on the student record sheet:	UA 066 862
Studienrichtung lt. Studienblatt | Degree programme as it appears on the student record sheet:	Masterstudium Chemie
Betreut von | Supervisor:	Assoz. Prof. Robert Woodward Ph.D.

Abstract

Hypervernetzte Polymere (HCPs) können aufgrund ihrer geringen Kosten, einfachen Synthese, großen spezifischen Oberfläche, permanenten und anpassbaren Porosität sowie ausgezeichneten chemischen und thermischen Stabilität als Adsorbentien zur Trennung organischer Schadstoffe aus Wasser und Abwasser verwendet werden. Die Einführung von Fluor in HCPs-Netzwerke verbessert die potenzielle Adsorption von Fluorchlorkohlenwasserstoffen durch Ausnutzung der Halogen-Halogen-Wechselwirkung sowie die Trennung von Öl (organischen Stoffen) von Wasser aufgrund der durch Fluor induzierten Hydrophobie. In dieser Arbeit haben wir eine Bibliothek fluorierter HCPs erstellt, wobei wir entweder 4,4′-Bis(chlormethyl)biphenyl (BCMBP) oder α,α′-Dichlor-p-xylol (pDCX) als Monomer und 4-Fluorbenzylchlorid (pFBC) oder Benzotrifluorid (BTF) als fluorhaltiges Monomer verwendet haben. Die Monomerverhältnisse wurden in den Polymeren, die mithilfe einer Friedel-Crafts-Alkylierungsreaktion synthetisiert wurden, systematisch variiert. Alle fluorierten HCPs wiesen hohe spezifische Oberflächen, gute thermische Stabilität und ausgezeichnete Beständigkeit gegen organische Lösungsmittel und Wasser auf. Darüber hinaus ließ sich ihr Fluorgehalt leicht steuern durch einfaches Variieren die Konzentration des fluorhaltigen Monomers während der Polymerisation. Unter den HCPs wies jedoch das Produkt BFHCP100, das auf der Selbstkondensation von BCMBP basiert und kein Fluor enthält, die höchste spezifische Oberfläche (1748 m^2/g) und die beste Öladsorptionskapazität gegenüber allen gemessenen organischen Lösungsmitteln auf (max. 15,23 g/g gegenüber 1,2-Dichlorethan) und erreichte eine Öl-/Wassertrennungseffizienz von über 99 %. Die Netzwerke zeigen Potenzial für die Behandlung von Abwässern mit organischen Schadstoffen und legen nahe, dass die Einbeziehung von Fluor in HCPs keinen Vorteil für die organische Adsorption brachte.

Abstract

Hypercrosslinked polymers (HCPs) can be used as adsorbents to separate organic pollutants from water and wastewater due to their low cost, facile synthesis, high specific surface area, permanent and tunable porosity, and excellent chemical and thermal stability. The introduction of fluorine into HCPs networks enhances potential chlorofluorohydrocarbons adsorption, by utilizing the halogen-halogen interaction, as well as the separation of oil (organics) from water due to the fluorine-induced hydrophobicity. In this work, we prepared a library of fluorinated HCPs, using either 4,4′-bis(chloromethyl)biphenyl (BCMBP) or α,α′-dichloro-p-xylene (pDCX) as monomer, with 4-fluorobenzyl chloride (pFBC) or benzotrifluoride (BTF) as fluorine-containing monomer. Monomer ratios were varied systematically throughout the polymers, which were synthesized using a Friedel-Crafts alkylation reaction. All fluorinated HCPs exhibited high specific surface areas, good thermal stability and excellent resistance to organic solvents and water. Further, their fluorine contents were easily controlled by simply varying the concentration of fluorine-containing monomer upon polymerization. Among the HCPs, however, the product BFHCP100, based on the self-condensation of BCMBP and containing no fluorine, displayed the highest specific surface area (1748 m2/g) and best oil adsorption capacities toward all measured organic solvents (max. 15.23 g/g toward 1,2-dichloroethane), achieving an oil/water separation efficiency of over 99%. The networks show potential for the treatment of wastewater containing organic pollutants and suggest that the inclusion of fluorine in HCPs did not impart benefit for organic adsorption.

Contents

1. Introduction

Water is an essential resource for human survival, sanitation, production and daily life. Unfortunately, hundreds of organic pollutants, originating from domestic sewage, industrial and agricultural wastewater, oil spills and leakage of septic tanks, have been found to contaminate water [1-6]. Common organic pollutants include pesticides, herbicides, fertilizers, long chain aliphatic hydrocarbons, phenols, plasticizers, polycyclic aromatic hydrocarbons (PAHs), detergents and surfactants, petroleum and crude oils, greases, pharmaceuticals and drugs, plastics, organic solvents, dyes, and even excreta of animals and human beings, etc. [1, 4-10]. These pollutants cause lasting damage to humans and aquatic ecosystems via bioaccumulation and biomagnification due to their strong lipophilicity and stability [3, 5, 11, 12]. To treat the organic contaminations in water and wastewater, numerous techniques and approaches have been developed, e.g., coagulation [13-16], membrane separation and filtration [10, 17], precipitation [18], ozonation [17], adsorption [1, 2], ion exchange [15, 19, 20], reverse osmosis [21], ultrasonication [22, 23], advanced oxidation processes [13, 14], biological [9, 24-27] and electrochemical treatment [13, 28]. The combination of different approaches and the fabrication of a product with multiple functions have been investigated in-depth [10, 13-15, 17, 18], in attempts to remove complex organic pollutants from water efficiently.

Advanced oxidation processes (AOP) are reactions to generate chemical oxidizing agents (mostly hydroxyl radicals (HO•)) capable of oxidative mineralizing and degrading the objective organic pollutants via hydroxylation, dehydrogenation and redox reactions [13, 29]. Hydroxyl radicals are efficiently produced chemically via a simple redox reaction, in which Fe^{2+} is oxidized to Fe^{3+} and H_2O_2 is reduced to the hydroxide ion and the desired hydroxyl radical, the so-called (thermal) Fenton reaction in Equation (1):

$$Fe^{2+}+H_2O_2 \rightarrow Fe^{3+}+OH^-+HO\bullet \quad (1)$$

In principle the affording Fe^{3+} from Equation (1) can be reduced back to Fe^{2+} by a second molecule of H_2O_2, but the reaction rate is much lower. Hence, stoichiometric amounts of Fe^{2+} are required to degrade the objective organic pollutants in the thermal Fenton reaction [13, 29]. To improve the reduction rate of Fe^{3+}, electro(catalytic)-Fenton and photo(catalytic)-Fenton have been developed, resulting in less iron dosage requirement. Besides, as shown in Equation (1), the Fenton reaction yields hydroxide ions which significantly increase the pH of the solution, leading to the formation of insoluble $Fe(OH)_3$ in water and thus the loss of iron dosage. Therefore, it is required to keep the system at low pH in the Fenton process, somewhat hindering its full-scale application [13]. Peroxicoagulation process is the combination of electro-Fenton and electrocoagulation processes, possessing the advantages of them both and valid for both low- and high-pH systems. Brillas et al. [30] reported the degradation of aniline by the peroxicoagulation process, which allows the removal of over 95% of aniline at a concentration of 1000 ppm at a current of 20 A within 5 h. In this process, the sacrificial iron anode was used to supply Fe^{2+} required for the Fenton reaction and the oxygen diffusion cathode was used to synthesize H_2O_2. Fe^{2+} reacted with H_2O_2, generating hydroxyl radicals and the excess of Fe^{2+} was oxidized to Fe^{3+}, forming precipitates as $Fe(OH)_3$. Aniline was removed by the synergetic effect of the degradation by attack of hydroxyl radicals and coagulation with $Fe(OH)_3$. The formation of recalcitrant intermediates is also a limitation of the Fenton reactions. For example, the electro-Fenton treatment of aromatic pollutants in water leads to the formation of short-chain carboxylic acids, which are resistant to the

attack of hydroxyl radicals, resulting in a slower degradation rate in the final stage of the process and thus a longer total mineralization time and a higher energy cost [31].

Ozonation is another powerful oxidizing process in AOP. Ozone electrophilically attacks atoms with a negative charge or C-C, C-N and N-N multiple bonds in the target compounds, and also reacts with water to form hydroxyl radicals. The combination of ozonation with other AOP improves the degradation efficiency of organic pollutants. Li et al. [32] prepared TiO_2 films by a sol–gel method and attached them to the inner wall of a tubular photoreactor. Test solutions containing 15.0 mg/L dibutyl phthalate were irradiated by a coaxial UV source while ozonized oxygen was continuously bubbled into the solutions through a porous glass plate. By the combination of TiO_2 films, UV light and ozone (TiO_2/UV/O_3), the degradation efficiency of dibutyl phthalate exceeded 90% within 30 min when the ozone dosage was 12.5 mg/h. When ozone dosage was increased to 50.0 mg/h, the removal rate of total organic carbon (TOC) was over 85% within 30 min. With the same concentration of ozone, the mineralization rate constants of dibutyl phthalate using TiO_2/UV/O_3 were 1.2–1.8 times higher than that using UV/O_3 and 3.5 times higher than that using TiO_2/UV.

Membrane separation and filtration are effective methods for removing organic pollutants from water based on the size-exclusion. Polymeric membranes dominate current water and wastewater treatment techniques; however, they may degrade under extreme environments (e.g., extremely acidic/basic conditions or extremely oxidative conditions). Compared to polymeric materials, ceramic membranes exhibit higher flux and better thermal, mechanical and chemical stability and allows for the combination of membrane separation with AOP, increasing the removal efficiency of the organic pollutants [10, 17]. Wang et al. [33] fabricated the flexible MnO_2@SiO_2 nanofibrous membranes (NFM) by combining electrospun SiO_2 nanofibers with hydrothermal synthesis. The material degraded 95% of methylene blue (MB) at the initial concentration of 10 mg/L within 40 min, assisted by the oxidation of H_2O_2. The membrane fouling and blinding caused by the deposition of organic pollutants, resulting in the decreasing permeate flux and increased operating costs, remains a challenge in the development of membrane filtration [10, 17].

Reverse osmosis (RO) is a special class of membrane filtration. In the RO process, hypertonic liquid (e.g., seawater or wastewater containing pollutants) and hypotonic liquid (e.g., distilled water) are separated by a semipermeable membrane. When pressure is applied to the hypertonic side (feed side), due to the limitation of the pore size or the surface charge of the membrane, only some molecules (e.g., water) can pass through the membrane and flow into the hypotonic side, while the solutes are retained in the hypertonic liquid. Xu et al. [34] reported the rejection of the hydrophilic ionic (e.g., ibuprofen), hydrophilic non-ionic (primidone), and hydrophobic non-ionic (bromoform, chloroform) organic pollutants using RO, nanofiltration (NF) and ultra-low-pressure reverse osmosis (ULPRO) membranes. At a target compound concentration of 300 ng/L, the rejection efficiencies of the RO membrane toward the hydrophilic ionic and hydrophilic non-ionic compounds exceeded 90%, while the rejection efficiencies toward bromoform and chloroform were 90% and 80%, respectively, poorer than those of the NF and ULPRO membranes. The high initial investment and operating cost in the RO process lead to its economic unfavorability [1].

Ultrasonic treatment is a new method for the degradation of organic pollutants in water. An abundance of tiny bubbles form when a specific frequency and intensity of ultrasonic irradiation is applied to a liquid and these bubbles lead to a series of physical and chemical changes during their formation, oscillation, growth, and collapse. The ultrasonic chemical reactions are mainly based on this effect, the so-called cavitation of ultrasound [22]. According to the hot spot theory, when the formed

bubble collapses, an instantaneous hot spot of up to 5000 K and 1000 atm is generated in a small area in and around the bubble in a very short period, affording small molecules and radicals (e.g., hydroxyl radicals). The resulting hydroxyl radicals further oxidatively mineralize the organic compounds. Additionally, in the transition zone between bubbles and solution, water is in a supercritical state. The non-volatile organic compounds are soluble in supercritical water and react with oxygen [22]. Sancheti et al. [23] synthesized NiO impregnated on CeO_2 catalyst with the assistance of ultrasound and its surface area increased from 31 to 95 m^2/g, compared to that synthesized using a conventional approach. The degradation efficiency of this catalyst in the treatment of Brillant Green dye at a concentration of 10 mg/L reached 46% within 4 h assisted by ultrasound irradiation, superior to the 21% degradation efficiency using the conventional catalyst. Degradation efficiency could be further improved to 82% with the new catalyst when coupled with UV light. Currently, ultrasonic treatment of organic pollutants is still at the stage of basic research, mainly in small-scale experiments in the laboratory and needs to be further expanded to large-scale industrial applications [22].

Biological treatment refers to the use of microorganisms (including aerobic and anaerobic fungi and bacteria) to degrade biodegradable organic pollutants in water [24-26]. One difficulty that plagues the application of biological treatment is the environmental sensitivity of microorganisms [26]. For example, high salinity (over 5-10 g/L chloride) reduces the degradation efficiency of microorganisms, making saline wastewater unsuitable for traditional biological treatment. To solve this problem, people have attempted to develop halotolerant bacterial strains. Arulazhagan et al. [27] utilized a halotolerant bacterial consortium consisting of *Ochrobactrum sp.*, *Enterobacter cloacae* and *Stenotrophomonas maltophilia* isolated from a marine environment to degrade 95% of PAHs (at a max. initial concentration of 100 ppm) within 4 days at a NaCl concentration of 30 g/L. However, when the NaCl concentration increased to 60 g/L, its degradation efficiency decreased to 39-45%.

Compared to the other water treatment techniques, adsorption is considered promising due to its simple design, low cost, facile operation, wide range of adsorbate scopes and highly efficient separation [1, 2]. When a substance contacts with solid surface (especially highly porous materials), the interaction between the substance and solid molecules results in the enrichment and accumulation of some molecules on the solid surface, a phenomenon known as adsorption [1, 2, 35]. The substance enriched on the solid surface during adsorption is called adsorbate, and the solid that enriches the substance is called adsorbent. A wide variety of porous materials have been studied and used as adsorbents, consisting of natural and modified or treated natural adsorbents as well as synthesized adsorbents [1], e.g., charcoal [36-38], clays [39, 40], plant materials and celluloses [41-43], sea materials [44], zeolites [45-47], ore minerals [48], industrial wastes [49, 50], graphene and carbon nanotubes [51, 52], silica [53-55], metal–organic frameworks (MOFs) [56-58], covalent organic frameworks (COFs) [6, 59], hypercrosslinked polymers (HCPs) [60-66] and other porous polymers [67, 68]. Srivastava et al. [69] produced a cheap carbonaceous adsorbent, using waste slurry from local fertilizer plants as raw material. Batch adsorption of 2,4-dinitrophenol was attempted using the carbon, removing 98% of the adsorbate at a concentration of $<5\times10^{-4}$ M and 68% removal of the adsorbate at a concentration of 1×10^{-3} M. The (commercial) ion-exchange resins are also common adsorbents used for the adsorption of organic pollutants containing ionizable groups. For example, Bayer anion exchange resin S6328a containing quaternary amine and trimethylamine groups was used for the adsorption of the reactive azo dyes RB5 and RR198 containing sulfonate groups and displayed the dye binding capacities 694.25 and 590.50 mg/g [70], respectively. However, the applications of ion exchange resins can be limited by high cost, degradation and disposal problems, and restricted performance conditions [20].

HCPs, as a branch of porous organic polymers (POPs), are a class of microporous (pore width smaller than 2 nm [71, 72]) and mesoporous (pore width between 2 and 50 nm [71, 72]) polymers synthesized primarily through acid-catalyzed Friedel–Crafts reactions. HCPs have been developed and used as adsorbents in water treatment in recent years due to the advantages of their tunable porosity, high specific surface area, excellent chemical and thermal stability, low density, wide and low-cost monomer sources, mild and simple synthesis, and facile post-functionalization [73-75]. HCPs were first introduced by Davankov and Tsyurupa in the 1970s, prepared through post-crosslinking of preformed linear polystyrene or lightly-crosslinked poly(styrene-co-divinylbenzene) using a bifunctional crosslinking agent [76]. The formed hypercrosslinked polystyrene are thus called "Davankov-type resins", possessing better organic adsorption performance than traditional gel-type or macroporous polystyrene. Pan et al. [77] reported the synthesis of particulate adsorbent NDA-701 via chloromethylation and post-crosslinking of styrene-co-divinylbenzene copolymer with chloromethyl methyl ether. Both batch and flow-through adsorption techniques on NDA-701 were used to treat wastewater from a chemical plant containing 4-nitrophenol, reducing its concentration from c. 5700 mg/L to below 0.5 mg/L in batch, and achieving a 348 mg/g breakthrough adsorption capacity, superior to two widely used adsorbents in the field, namely a macroporous polymeric adsorbent (Amberlite XAD-4) and a commercial activated carbon (GAC-1). Moreover, the 4-nitrophenol-loaded NDA-701 was regenerated entirely using NaOH solution, higher than the reported 75% regeneration efficiency of GAC-1. Zeng et al. [78] prepared macroporous styrene-co-divinylbenzene copolymer with ester groups by suspension polymerization, followed by a Friedel-Crafts-based post-crosslinking of its pendant vinyl groups, producing bead-shaped adsorbent PDM-2. The resulting dry resin was wetted with aqueous phenol solution, packed in a glass column and displayed 52.6 mg/mL breakthrough adsorption capacity and 55.8 mg/mL total adsorption capacity toward phenol. Furthermore, almost 100% regeneration efficiency was achieved using a 3 BV industrial alcohol treatment at room temperature, from which both phenol and the alcohol can be recovered by distillation. Yang et al. [65] synthesized chloromethylated poly(styrene-co-divinylbenzene) beads, followed by modification with 2-hydroxyterephthalic acid. The generated adsorbent 2-HTA-HCP exhibited excellent adsorption performance toward both organic pollutants (amines, phenols and dyes), and heavy metal ions (Pb^{2+}, Hg^{2+}, and Cd^{2+}). Generally, the powdery, particulate or bead-shaped HCP adsorbents, like those mentioned above, exhibit higher specific surface area than those in other forms, while their oil adsorption capacities were limited [79]. This may be because when the powdered adsorbents are suspended in the solvent, they tend to spontaneously aggregate to reduce the surface energy, thereby losing effective surface areas. The regeneration of the powdered adsorbents was usually achieved with ethanol or ether, thus was expensive, inefficient, and environmentally unfriendly, hindering large-scale implementation in oil removal [79]. Xue et al. [61] fabricated superhydrophobic melamine formaldehyde materials, HMF, via the anchoring of benzene-based HCPs. Melamine (formaldehyde) sponge is a three-dimensional porous material and exhibits superhydrophilicity and underwater superoleophobicity (e.g., its adsorption capacity toward diesel oil in diesel oil/water mixture is 0 g/g [80]). However, when the HCPs are homogeneously coated on the melamine sponge, superhydrophobic materials with high surface areas are formed. The coated material HMF exhibited an oil adsorption capacity of 130 mL/g, a separation efficiency > 99%, and remarkable environmental resistance. Further, adsorbed oil was easily recycled by simply squeezing the HMF, which retained 45-50% recovery efficiency even after 10 cycles. Lin et al. [62] modified fluoro-poly(high internal phase emulsions) (F-PolyHIPEs) by hypercrosslinking using dimethoxymethane (FDA) as external crosslinker, yielding the

hierarchically porous monolithic adsorbent HCPF-PolyHIPEs. The specific surface area of HCPF-PolyHIPEs increased from 16 to 353 m^2/g after hypercrosslinking, and the resulting material displayed good adsorption performance toward organic solvents and CO_2. The regeneration of the HCPF-PolyHIPEs and the recovery of the adsorbed solvents were achieved via centrifugation.

Despite the extensive study of HCP adsorbents, some obstacles still hinder their large-scale industrial fabrication, such as the use of hazardous and harmful reagents (e.g. above-mentioned chloromethyl methyl ether) [78] or expensive noble metal-based catalysts [66] utilized in network synthesis, as well as heat and HCl generation in some hypercrosslinking processes [66, 74]. In addition, it is also a challenge to develop HCP adsorbents exhibiting selective adsorption performance.

Chlorofluorocarbons (CFCs) and chlorofluorohydrocarbons (HCFCs) are a class of fully or partly halogenated hydrocarbons and are used as refrigerants, blowing agents, insulation and packaging materials, and solvents [81]. CFCs and HCFCs enter groundwater via river water infiltration, landfills and industrial solvent spills [82]. Hence, it is necessary to synthesize a HCP adsorbent to specifically adsorb and remove them from water and wastewater. Luo et al. [83] reported the synthesis of a powdered adsorbent F-PDVB through the post-crosslinking of polydivinylbenzene using perfluorinated benzylic alcohols as crosslinker, yielding high surface area (771 m^2/g), impressive fluorine content (22%), and specific adsorption toward various CFCs. However, the adsorption capacities of F-PDVB must still be further improved (max. 5.20 g/g toward trichlorofluoromethane).

4,4′-Bis(chloromethyl)biphenyl (BCMBP) and α,α′-dichloro-p-xylene (pDCX) are common monomers in HCP synthesis and the specific surface areas of the HCPs from their self-polycondensation reach up to 1874 and 1431 m^2/g [84], respectively. Wood et al. [84] reported the synthesis of the HCPs based on the self-polycondensation and copolymerization of BCMBP and pDCX as well as their potential application in hydrogen storage. Martín et al. [85] produced a series of HCPs based on the self-condensation or copolymerization of BCMBP and pDCX as potential adsorbents for CO_2 capture, reaching a maximum CO_2 uptake of 7.4 wt.% at atmospheric pressure and 298 K. Schweng et al. [86] synthesized a robust and low-cost sulfonated HCP via the self-condensation and sulfonation of BCMBP with chlorosulfonic acid, used for atmospheric water harvesting. Hubert et al. [87] prepared the same sulfonated BCMBP-based HCP, followed by its electrophoretic deposition onto carbon fibres, to produce a structural composite supercapacitor. Sheng et al. [63] coated HCP on melamine formaldehyde sponge by the direct surface condensation of pDCX, followed by coating with polydimethylsiloxane (PDMS) as protection layer, fabricating a superhydrophobic adsorbent MF-HCP-PDMS, used for oil/water emulsion separation and oil recovery with ultrahigh separation efficiency and outstanding durability (>99% over 10 cycles in liter-scale experiments). Thus far, however, to the best of our knowledge there is no investigation reported about the oil adsorption performance of HCPs entirely produced from the self-polycondensation of BCMBP and pDCX.

In this work, we utilize the self-polycondensation of BCMBP and pDCX to form porous frameworks. We introduce two fluorinate-containing monomers independently, 4-fluorobenzyl chloride (pFBC) and benzotrifluoride (BTF), using different monomer ratios to afford a series of fluorinated HCPs, used as oil adsorbents in water treatment. By exploiting halogen-halogen interactions [88] and the hydrophobicity of fluorine [83, 89], we aim to enhance the specific adsorption performance of the generated HCPs toward HCFCs as well as the oil/water selectivity and separation efficiency simultaneously. Moreover, the network preparation process was simplified compared to many literature examples by the employment of a facile one step synthesis route.

2. Experimental Section

2.1. Materials

4,4′-Bis(chloromethyl)biphenyl (BCMBP), α,α′-dichloro-p-xylene (pDCX), $FeCl_3$, Sudan III (≥ 85%), 1,2-dichloroethane (DCE)(≥99.0%), methanol (≥99.8%), toluene (≥99.7%), n-heptane (≥ 99%) were purchased from Sigma-Aldrich. 4-Fluorobenzyl chloride (pFBC) and benzotrifluoride (BTF) were purchased from Tokyo Chemical Industry (TCI). All chemicals were used as received.

2.2. Hypercrosslinked polymer (HCP) synthesis

In a 50 mL double neck round bottom flask, monomers (details shown in Table 1) and 10 mL DCE were added in sequence. After stirring for 5 min to dissolve the monomers, $FeCl_3$ (0.243 g, 1.5 mmol, 1.5 eq.) was added, and the mixture refluxed at 80 °C for 14 h. After cooling to room temperature, the resulting solids were filtered with a Büchner funnel, washed with roughly 100 mL of methanol in portion and further cleaned by Soxhlet extraction with methanol for 22 h. Finally, the synthesized HCPs were placed in fumehood for 14 h to remove most of the solvent, grounded into fine powder using a pestle and mortar, and then further dried in a vacuum drying oven at 5 inHg and 80 °C for 14 h, yielding brown/dark brown powders. Additionally, the reactions were scaled up to 3 mmol (based on monomer 1) in a 100 mL double neck round bottom flask. It should be noted that, both BFHCP series and BTFHCP series are 4,4'-dimethylbiphenyl-based framework, so BFHCP100 is the same network in both series.

Table 1. Details about monomeric composition of all synthesized HCPs

Series	Product	Monomer 1		Monomer 2		Yields (%)	
		Name	n (mmol)	Name	n (mmol)	in 1 mmol	in 3 mmol
BFHCP	BFHCP100	BCMBP	1	pFBC	0	73	87
	BFHCP75				0.33	52	94 to 102
	BFHCP50				1	64	96 to 100
XFHCP	XFHCP100	pDCX	1	pFBC	0	72	102 to 120
	XFHCP75				0.33	94	110 to 115
	XFHCP50				1	82	103 to 105
BTFHCP	BTFHCP75	BCMBP	1	BTF	0.33	56	84
	BTFHCP50				1	48	55
Self-polycondensation of pFBC		pFBC	1	-	-	2	-

2.3. Characterization

2.3.1. Fourier-transform infrared (FTIR) spectroscopy

FTIR spectra of the synthesized samples and samples recycled after adsorption experiment were collected with a Tensor II FTIR spectrometer (Bruker) equipped with a Bruker Platinum-ATR Convenience sampling module at room temperature. Spectra were measured in the range of 400 to 4000

cm^{-1} with a resolution of 4 cm^{-1}, and were recorded and analyzed using the OPUS 7.5 software.

2.3.2. Thermogravimetric analysis (TGA)

TGA of the samples was investigated using a Discovery TGA (TA instruments). Roughly 3 to 5 mg of sample was placed into a TGA high-temperature platinum sample pan, equilibrated at 30 °C, then heated at a ramp rate of 10 °C/min up to 800 °C in air. Samples were held at the target temperature for 5 min before being allowed to cool. The TGA data were recorded and analyzed using the Discovery TGA @Lab program in TRIOS software.

2.3.3. X-ray photoelectron spectroscopy (XPS)

XPS spectra of the synthesized samples were determined on a Nexsa Photoelectron Spectrometer (Thermo Scientific) and all the measurements were performed using Al-Kα X-rays with a spot size of 400 μm. The survey spectra were taken at pass energy of 200 eV from 1350 to 0 eV with a resolution of 1 eV. The high-resolution C 1s, O 1s, F 1s and Cl 2p spectra were all collected at a pass energy of 50 eV with a resolution of 0.1 eV. C 1s was collected in the range from 298 to 279 eV, O 1s from 545 to 525 eV, F 1s from 698 to 678 eV, and Cl 2p from 210 to 190 eV.

2.3.4. Gas sorption isotherms

We used N_2 adsorption-desorption isotherms to evaluate the porous nature of the HCPs. The N_2 adsorption–desorption isotherms were measured with a TriStar II (Micromeritics) at −196 °C and recorded and analyzed by the software TriStar II 3020 3.02. Before the measurement, roughly 50 to 100 mg of sample was degassed at 120 °C under N_2 flow for 14 h using a FlowPrep 060 (Micromeritics).

The specific surface areas (SSA) of the samples were determined via the Brunauer–Emmett–Teller (BET) method in the relative pressure P/P_0 range 0.05 to 0.3.

The pore size distributions (PSDs) of the synthesized samples were determined from the N_2 adsorption branch of the isotherm. Non-local-density functional theory (NLDFT) model has been reported to determine the PSDs of HCPs [83], which was based on the assumption of the adsorption of fluids onto molecularly smooth surfaces and thus more valid for the characterization of ordered materials [90], but generally HCPs possessed amorphous structure [74, 75]. The difference between the assumption of a smooth and homogenous surface and the actual amorphous structure of HCPs resulted in imprecise PSDs and inaccurate volumes, especially in the micropore region [90]. Hence, in this work the quenched solid density functional theory (QSDFT) model was used to calculate the PSDs of the products, in which the roughness parameter was introduced to quantitatively evaluate the surface geometrical heterogeneity, obtaining more accurate results [72, 90]. The total pore volume V_P, micropore volume V_{Mic} and mesopore volume V_{Mes} were determined from the cumulative pore volumes calculated by QSDFT model in the range of pore width between 0 to 500 Å [71, 72].

2.4. Oil adsorption and oil/water separation experiment

To determine oil adsorption capacity, roughly 45 mg of sample was suspended in 10 ml of solvent in a covered 20 ml glass vail and stirred at 250 rpm for 1 h. After stirring, vacuum filtration was used to

remove excess solvent until no liquid dropped down from the Büchner funnel and the filter cake did not appear to regain moisture upon vacuum removal. Subsequently, the filter cake was weighed as soon as possible to reduce the influence of solvent evaporation and finally dried at 120 °C in a drying cabinet for 14 h and weighed again. Every measurement was repeated 5 times. The adsorption capacity k_D based on the weight of sample after drying was calculated as follows:

$$k_D = \frac{m_A - m_D}{m_D} \quad (2)$$

where m_A and m_D were the weight of the sample after adsorption and after drying, respectively.

As comparison, the adsorption capacity k_B based on the weight of sample before adsorption was calculated too, according to the following equation reported in references [38, 54, 61-63, 67]:

$$k_B = \frac{m_A - m_B}{m_B} \quad (3)$$

where m_B was the weight of the sample before adsorption.

To demonstrate the feasibility of immiscible organic solvent removal from water using HCPs, toluene and distilled water were selected as organic and aqueous phase, respectively, in the oil/water separation experiment. To visualize the separation, toluene was dyed using fat-soluble dye Sudan III at a concentration of 0.01 g/mL. The oil/water mixture was prepared in a 25 mL graduated cylinder using 0.5 mL of Sudan III dyed toluene and 20 mL of distilled water, followed by the addition of samples in portions while shaking gently until no liquid red organic phase could be observed. The toluene-loaded samples were removed from solution by vacuum filtration and the oil/water separation efficiency SE was calculated in the following equation reported by Sarkar et al. [91]:

$$SE = \frac{m_{Wr}}{m_{Wi}} \times 100\% \quad (4)$$

where m_{Wi} and m_{Wr} were the initial weight of water and weight of recycled water after separation, respectively. The adsorption efficiency AE of samples during oil/water separation was calculated using Equation (5):

$$AE = \frac{m_{St}}{m_{Sa}} \times 100\% \quad (5)$$

where m_{St} and m_{Sa} were the theoretical (based on their adsorption capacities) and actual dosages of the samples in the separation experiment, respectively. Additionally, 20 mL of water alone was used as a control to measure any potential loss during vacuum filtration. The control was repeated 5 times.

3. Results and Discussion

3.1. Synthesis of HCPs

We successfully synthesized three series of HCPs in this work, namely BFHCP series, XFHCP series and BTFHCP series (Scheme 1). Networks were produced using various monomer ratios via Friedel-Crafts benzylation catalyzed by $FeCl_3$, in which the polymer formation and fluorine introduction were combined into one step, resulting in facile and economic procedure. Among these HCPs, the BFHCP series were prepared with the monomer ratios of BCMBP:pFBC (n:n) = 100:0, 75:25 and 50:50, affording the corresponding powdery products BFHCP100, BFHCP75 and BFHCP50, respectively (Scheme 1a). The XFHCP series were prepared with the monomer ratios of pDCX:pFBC (n:n) = 100:0, 75:25 and 50:50, affording the corresponding powdery products XFHCP100, XFHCP75 and XFHCP50, respectively (Scheme 1b). Finally, the BTFHCP series were prepared with the monomer ratios of BCMBP:BTF (n:n) = 75:25 and 50:50, affording the corresponding powdery products BTFHCP75 and BTFHCP50 (Scheme 1c). Further synthesis details are provided in the Experimental Section. We also attempted the self-polycondensation of pFBC under the same reaction conditions as in HCP synthesis, however, poor yields (2%, Table 1) demonstrated the inefficiency of the reaction in this case. The yields of BFHCP series and XFHCP series in 1 mmol-scale (based on BCMBP and pDCX, respectively) ranged from 52% to 94%, and raised to a maximum of 120% in 3 mmol-scale synthesis (Table 1), caused by the higher residual terminal chlorine in the 4,4'-dimethylbiphenyl or p-xylene framework. In contrast, the yields of the BTFHCP series were lower (for BTFHCP75 56% in 1 mmol-scale reaction and 84% in 3 mmol-scale reaction, for BTFHCP50 48% in 1 mmol-scale reaction and 55% in 3 mmol-scale reaction), as the reaction was deactivated by the trifluoromethyl substituent group due to its strong inductive electron-withdrawing effect.

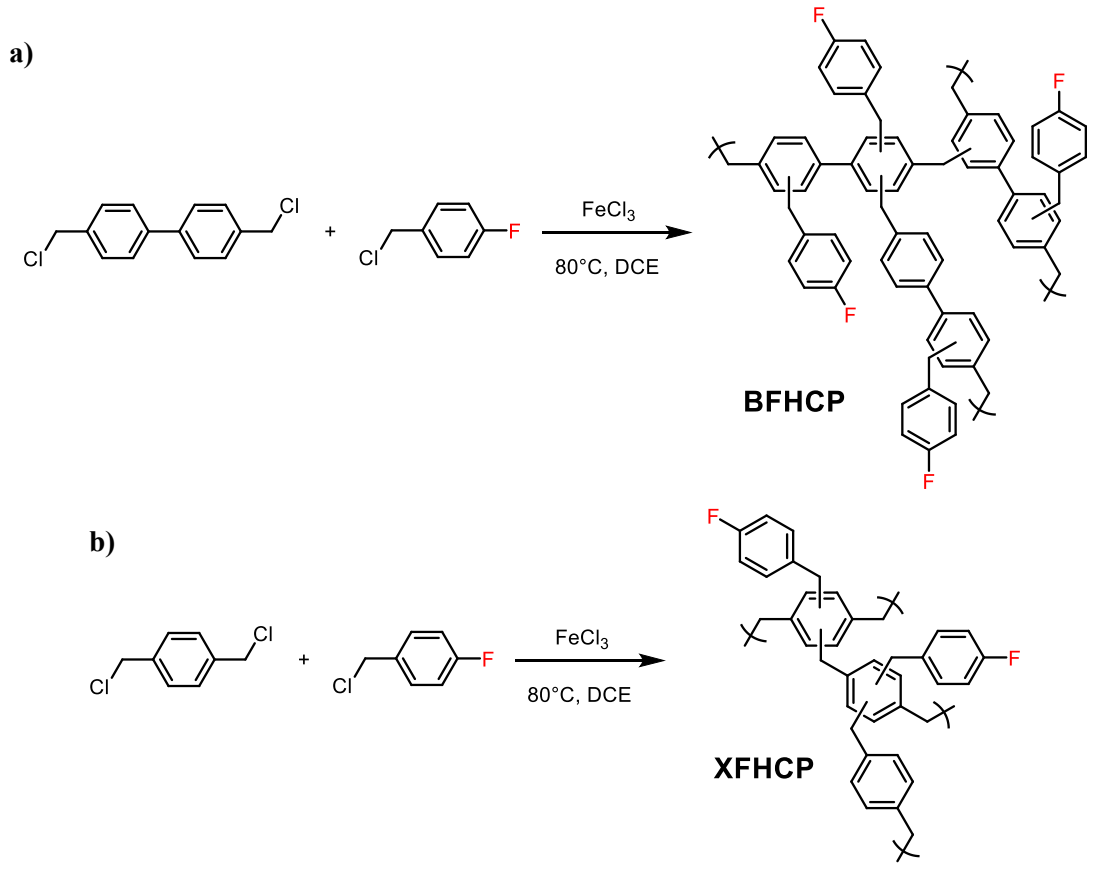

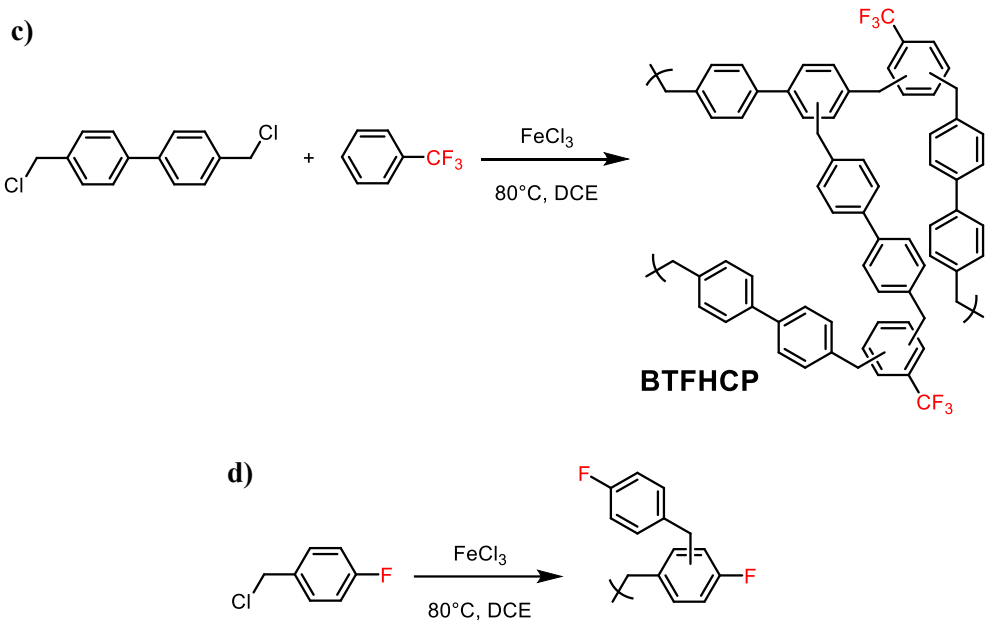

Scheme 1. Synthesis of (a) BFHCP series, (b) XFHCP series and (c) BTFHCP series, as well as (d) self-polycondensation of pFBC.

3.2. Characterization of synthesized HCPs

The chemical properties of the HCPs were characterized with FTIR spectroscopy and XPS. Physical properties, including porosity and thermal stability, were determined using N_2 gas sorption analysis and TGA, respectively.

3.2.1. FTIR spectroscopy

The FTIR spectra of the BFHCP series (Figure 1a) displayed the characteristic absorption peaks of the 4,4'-dimethylbiphenyl framework in BFHCP100 as well as three new peaks in both BFHCP75 and BFHCP50 at 1228, 1157 and 501 cm^{-1}, due to the introduction of p-fluorobenzyl group into the framework. The peaks at 1228 and 1157 cm^{-1} were assigned to C-H in-plane bending vibration in the fluorinated aromatic ring and the peak at 501 cm^{-1} was assigned to the characteristic C_{Ar}-F bending vibration [92]. The characteristic peak of C_{Ar}-F stretching vibration at around 1330 cm^{-1} [92] was likely overlaid by other peaks due to its weak intensity, and so it was not observed in the FTIR spectra of BFHCP75 and BFHCP50. All the new peaks introduced upon the inclusion of pFBC increased in intensity with increasing monomer ratio, indicating the higher fluorine content in BFHCP50 compared to BFHCP75. A similar trend was observed in the FTIR spectra of the XFHCP series (Figure 1b). Three new peaks appeared in the spectra of XFHCP75 and XFHCP50 compared to XFHCP100 at 1233, 1157 and 501 cm^{-1}, similar to corresponding peaks in the BFHCP series and confirming the successful introduction of pFBC. Furthermore, the increasing intensity of the three new peaks over the pFBC monomer ratio again indicated the highest fluorine content in XFHCP50 among the XFHCP series. In the FTIR spectra of the BTFHCP series, three new peaks appeared in BTFHCP75 and BTFHCP50 at 1329, 1135 and 702 cm^{-1} (Figure 1c) , in good agreement with the three adsorption peaks at 1324, 1126 and 694 cm^{-1} in the IR spectrum of BTF monomer [93]. BTFHCP50 appeared to have the highest

fluorine content among the BTFHCP series, displaying the largest intensity of the three emergent peaks in its FTIR spectrum. Therefore, in all three series, the fluorine appeared to be successfully introduced into the framework using Friedel-Crafts benzylation, and its content increased with increasing ratios of fluorine-containing monomer.

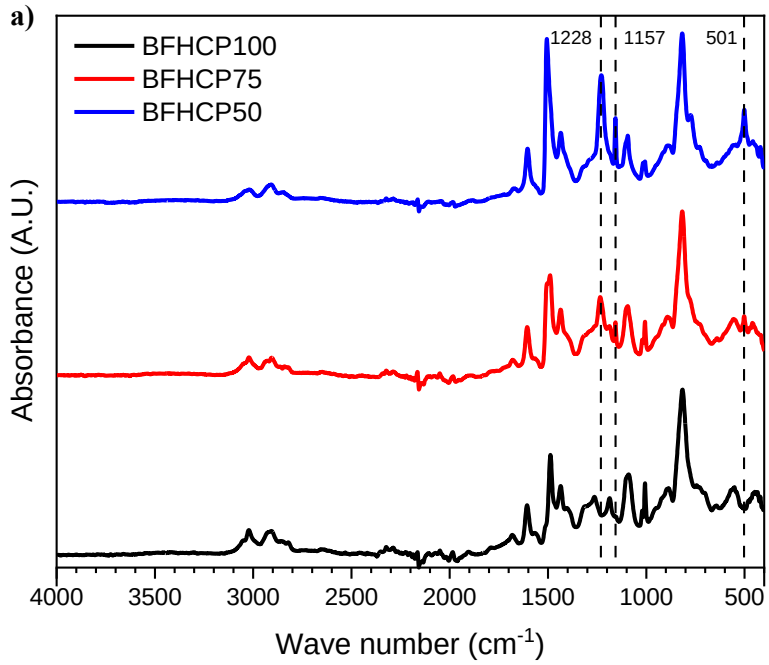
a)
BFHCP100
BFHCP75
BFHCP50
1228
1157
501
Absorbance (A.U.)
4000
3500
3000
2500
2000
1500
1000
500
Wave number (cm-1)

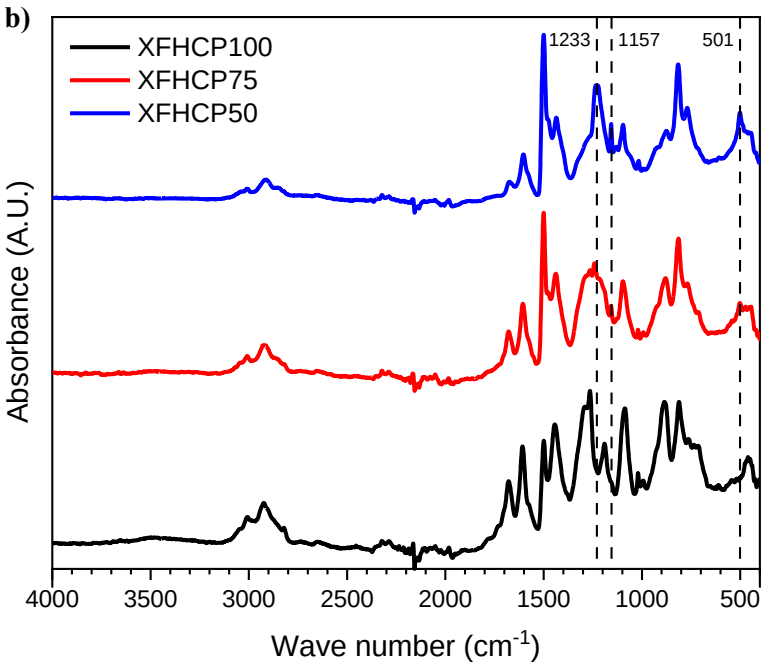
b)
XFHCP100
XFHCP75
XFHCP50
1233
1157
501
Absorbance (A.U.)
4000
3500
3000
2500
2000
1500
1000
500
Wave number (cm-1)

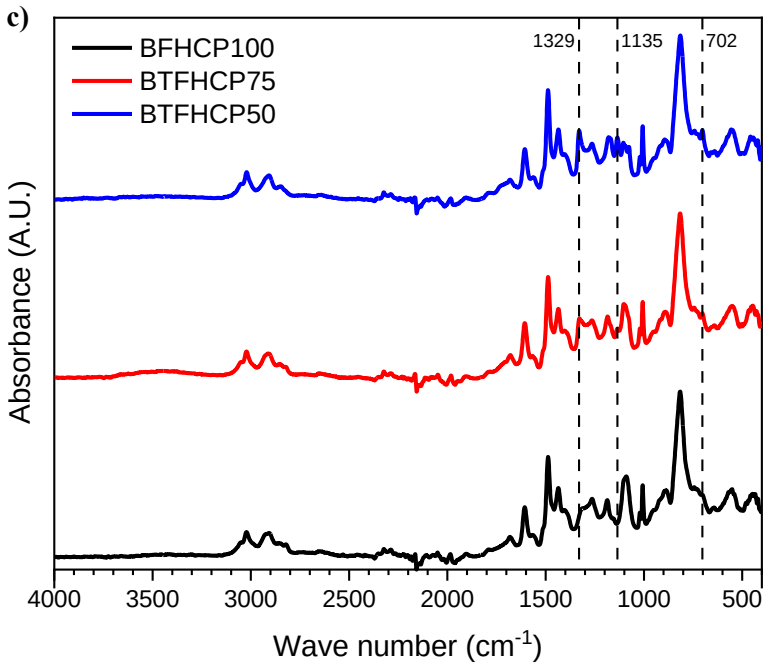

Figure 1. FTIR spectra of (a) BFHCP series, (b) XFHCP series and (c) BTFHCP series.

3.2.2. TGA

The TGA curves of the BFHCP series presented striking similarity (Figure 2a). All the polymers were slightly oxidized at around 240 to 260 °C, indicated by a weight increase to slightly above 100%, before the onset of thermal decomposition at around 340 to 360 °C, demonstrating excellent thermal stability of BFHCP series. All samples were decomposed completely at around 580 to 600 °C. The introduction of fluorine into the 4,4'-dimethylbiphenyl framework did not significantly change their thermal stability, which may be explained by the small difference between the bond energy of C-F bond (485 kJ/mol [94]) and the average bond energy in the aromatic ring (474 kJ/mol) of C-C bond (346 kJ/mol [94]) and C=C bond (602 kJ/mol [94]). The TGA curves of the XFHCP series (Figure 2b) and the BTFHCP series (Figure 2c) displayed almost identical curves with the BFHCP series, also demonstrating their excellent thermal stability.

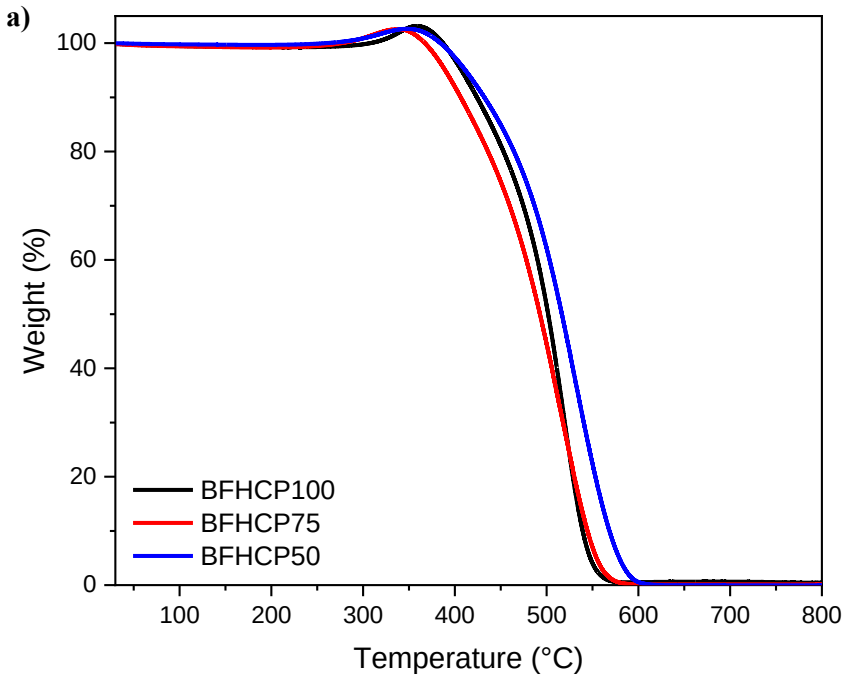
a)
Weight (%)
Temperature (°C)
BFHCP100
BFHCP75
BFHCP50

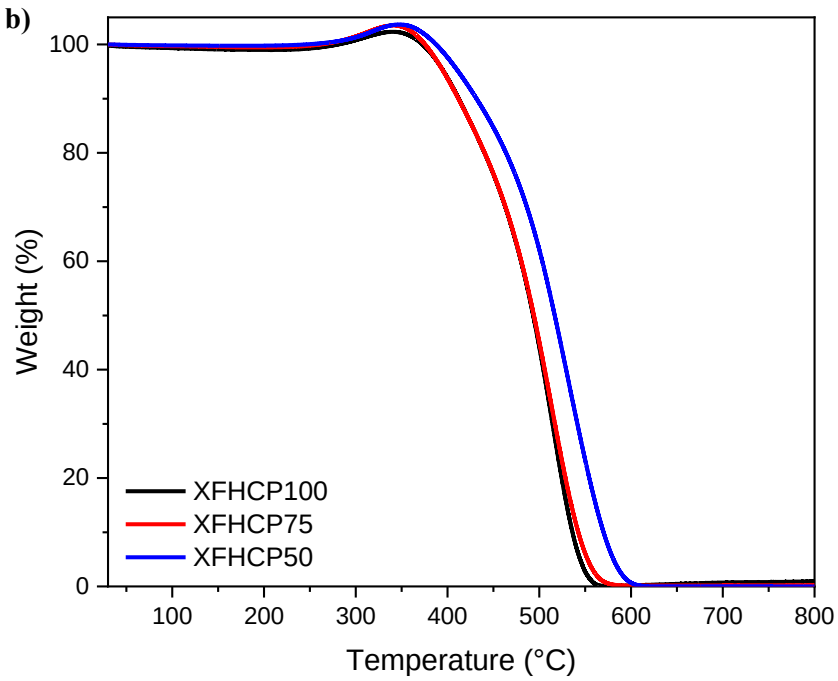
b)
Weight (%)
Temperature (°C)
XFHCP100
XFHCP75
XFHCP50

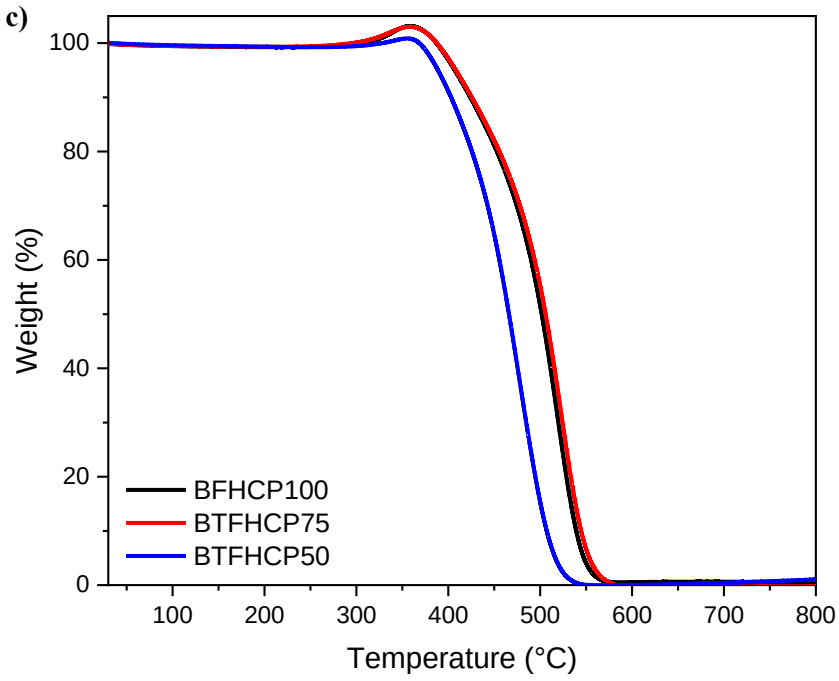

Figure 2. TGA curves of (a) BFHCP series, (b) XFHCP series and (c) BTFHCP series.

3.2.3. X-ray photoelectron spectroscopy (XPS)

XPS was performed to detect the presence and relative content of fluorine in all HCPs. As shown in the XPS spectra (Figure 3a to 3c), the characteristic peaks at binding energies within the ranges 687.15 to 690.20 eV (F 1s), 532.42 to 532.61 eV (O 1s), 284.49 to 284.86 eV (C 1s), and 201.52 to 200.76 eV (Cl 2p) [83, 95], show the presence of fluorine in all fluorinated HCPs, namely BFHCP75, BFHCP50, XFHCP75, XFHCP50, BTFHCP75 and BTFHCP50, as well as the presence of residual terminal chlorine in all HCPs. The trace fluorine content in BFHCP100 and XFHCP100 could simply be due to some slight sample cross-contamination during measurement. The presence of oxygen in all HCPs was ascribed to the introduction of oxygen in the synthesis process under air atmosphere due to the attack of water vapor at the carbocation generated during the Friedel-Crafts reaction. The FTIR spectra of the BFHCP series after being stored in air for 6 months were almost same with their corresponding pristine spectra (Figure 4a to 4c), confirming the excellent stability of HCPs in ambient conditions and ruling out post-synthetic oxidation.

Measured fluorine to carbon atomic ratios R_m were compared to theoretical fluorine to carbon atomic ratios R_t of the synthesized HCPs using Equation (6):

$$R = \frac{Atomic\ percentage\ of\ fluorine}{Atomic\ percentage\ of\ carbon} \times 100\% \quad (6)$$

R_m increased over pFBC monomer ratio from 0.1% to 7.0% and from 0.1% to 9.2% (Table 2a and 2b) in both BFHCP series and XFHCP series, respectively, quantitatively proving the results of their FTIR

spectra that BFHCP50 and XFHCP50 exhibited the highest fluorine content in each series. Interestingly, R_m was always larger than its corresponding R_t in fluorinated HCPs based on pFBC, namely BFHCP75, BFHCP50, XFHCP75 and XFHCP50, revealing a larger loss of BCMBP and pDCX in the synthesis. In BTFHCP75 and BTFHCP50, despite the higher fluorine content in BTF than that in pFBC, R_m was much lower than the corresponding R_t (Table 2c), explaining their low yields and demonstrating BTF as a poor monomer for fluorinated HCP synthesis.

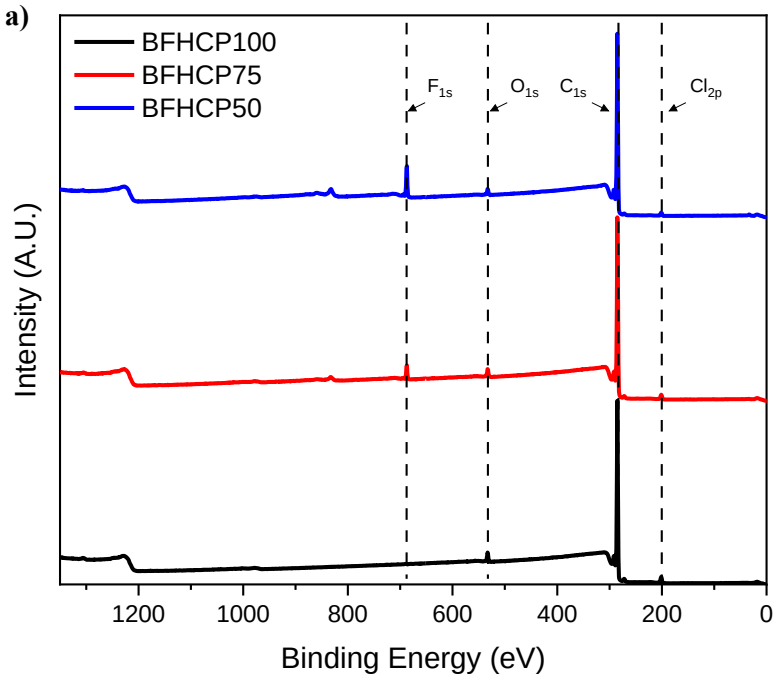

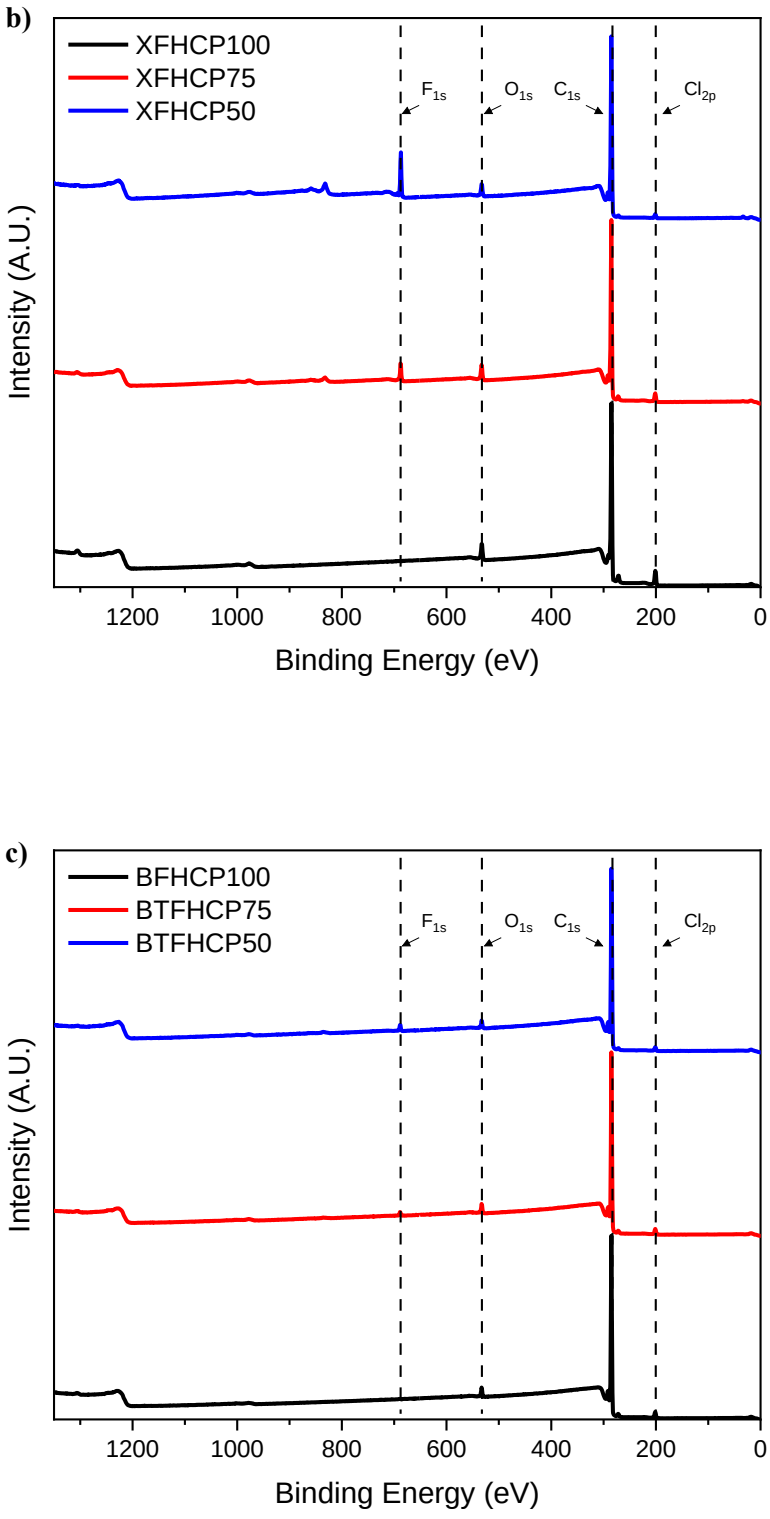

Figure 3. XPS survey spectra of (a) BFHCP series, (b) XFHCP series and (c) BTFHCP series.

Table 2. XPS data of the synthesized HCPs collected from survey spectra

a) BFHCP series

	Name	BFHCP100	BFHCP75	BFHCP50
C 1s	Binding energy (eV)	284.7	284.6	284.7
	FWHM (eV)	1.5	1.5	1.5
	Atomic percentage (%)	96.1	93.9	91.4
O 1s	Binding energy (eV)	532.6	532.5	532.5
	FWHM (eV)	2.1	2.3	2.2
	Atomic percentage (%)	2.5	2.2	1.6
F 1s	Binding energy (eV)	689.3	687.3	687.2
	FWHM (eV)	0.2	1.7	1.7
	Atomic percentage (%)	0.1	2.9	6.4
Cl 2p	Binding energy (eV)	200.7	200.7	200.6
	FWHM (eV)	2.7	2.7	1.6
	Atomic percentage (%)	1.4	1.0	0.7
	R_m (%)	0.1	3.1	7.0
	R_t (%)	0.0	2.4	4.8

b) XFHCP series

	Name	XFHCP100	XFHCP75	XFHCP50
C 1s	Binding energy (eV)	284.6	284.9	284.8
	FWHM (eV)	1.6	1.6	1.5
	Atomic percentage (%)	92.1	90.1	87.9
O 1s	Binding energy (eV)	532.4	532.6	532.5
	FWHM (eV)	2.8	2.6	2.7
	Atomic percentage (%)	4.9	4.1	3.2
F 1s	Binding energy (eV)	690.2	687.3	687.6
	FWHM (eV)	0.4	1.8	1.7
	Atomic percentage (%)	0.1	4.0	8.1
Cl 2p	Binding energy (eV)	200.5	200.8	200.6
	FWHM (eV)	1.7	2.6	1.6
	Atomic percentage (%)	2.9	1.8	0.8
	R_m (%)	0.1	4.4	9.2
	R_t (%)	0.0	3.2	6.7

c) BTFHCP series

	Name	BFHCP100	BTFHCP75	BTFHCP50
C 1s	Binding energy (eV)	284.7	284.6	284.5
	FWHM (eV)	1.5	1.5	1.5
	Atomic percentage (%)	96.1	95.4	95.6
O 1s	Binding energy (eV)	532.6	532.4	532.5
	FWHM (eV)	2.1	2.3	2.2
	Atomic percentage (%)	2.5	2.6	2.1
F 1s	Binding energy (eV)	689.3	688.4	688.3
	FWHM (eV)	0.6	1.9	2.0
	Atomic percentage (%)	0.1	0.8	1.4
Cl 2p	Binding energy (eV)	200.7	200.7	200.6
	FWHM (eV)	2.7	2.7	2.7
	Atomic percentage (%)	1.4	1.2	0.8
	R_m (%)	0.1	0.9	1.5
	R_t (%)	0.0	6.1	14.3

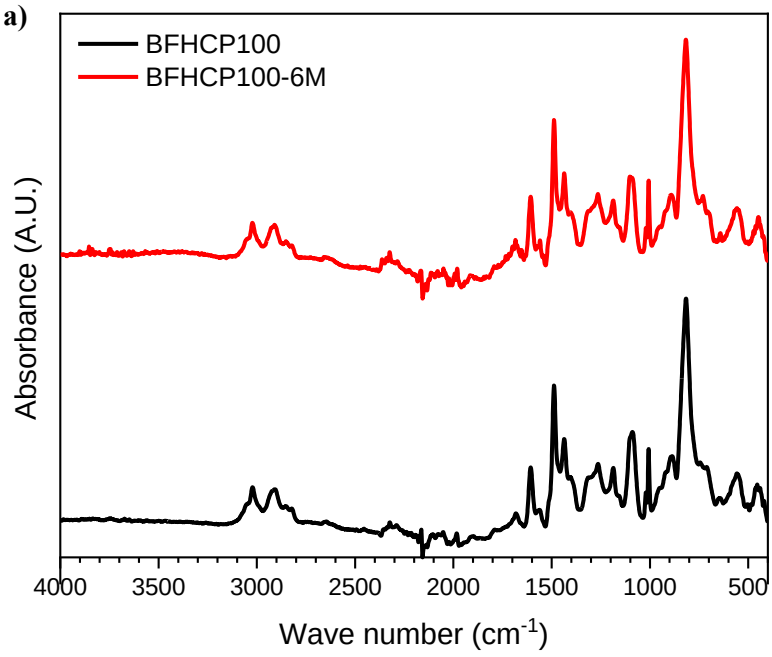
a)
BFHCP100
BFHCP100-6M
Absorbance (A.U.)
4000
3500
3000
2500
2000
1500
1000
500
Wave number (cm-1)

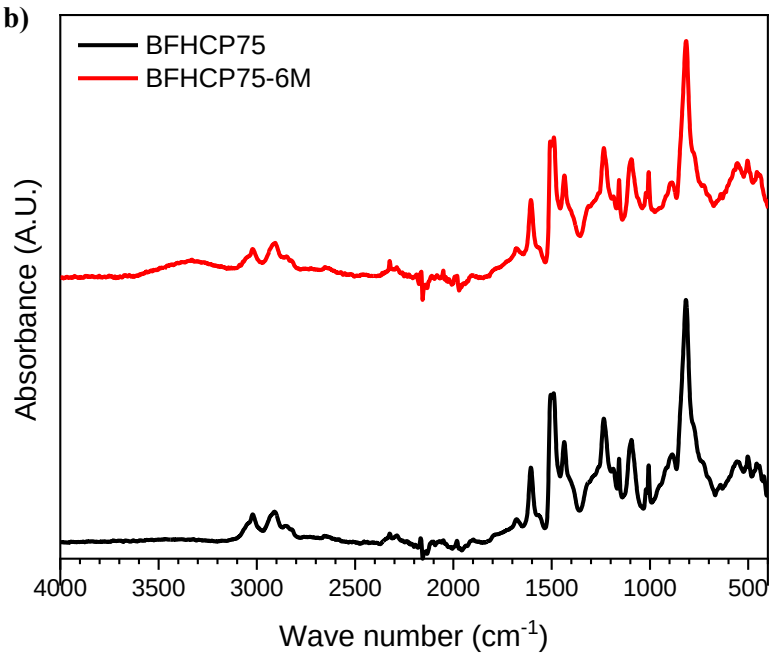
b)
BFHCP75
BFHCP75-6M
Absorbance (A.U.)
4000
3500
3000
2500
2000
1500
1000
500
Wave number (cm-1)

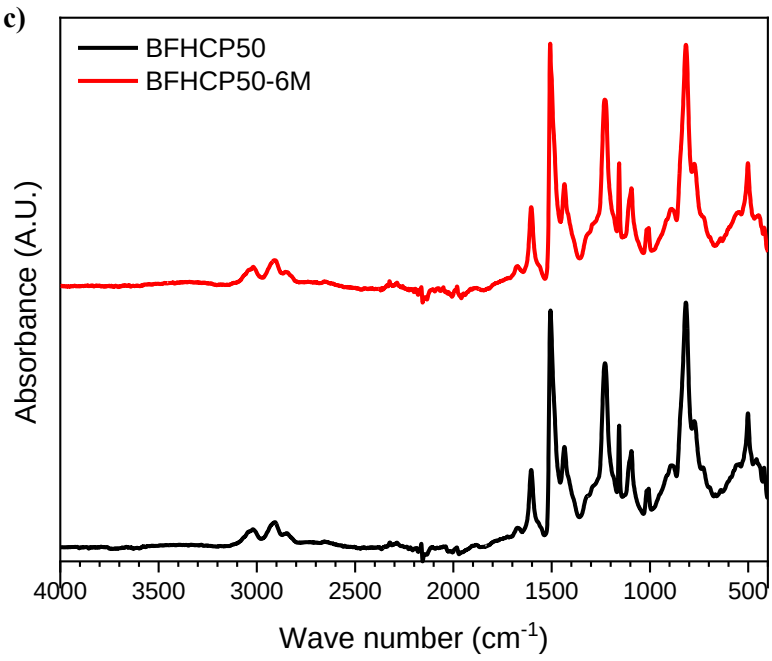

Figure 4. Comparison of the FTIR spectra of (a) BFHCP100, (b) BFHCP75 and (c) BFHCP50, before and after 6 months storage in air at room temperature, wherein 6M represents the samples after 6 months storage.

In the fluorinated BFHCP series and XFHCP series, the peaks at 687.5 eV of binding energy in the F 1s region were assigned to C_{Ar}-F in p-fluorobenzyl group and in fluorinated BTFHCP series, the peaks at 688.7 eV were assigned to CF_3 in BTF (Figure 5b, 5c and 5e to 5h) [95]. Additional peaks in the F 1s region at roughly 694 eV were observed in almost all fluorinated HCPs, which cannot be assigned to any known C-F. These peaks are close to the binding energy of SF_6 (693.5 eV) in the F 1s region according to a database [95], but the reason for their appearance in this work is unknown.

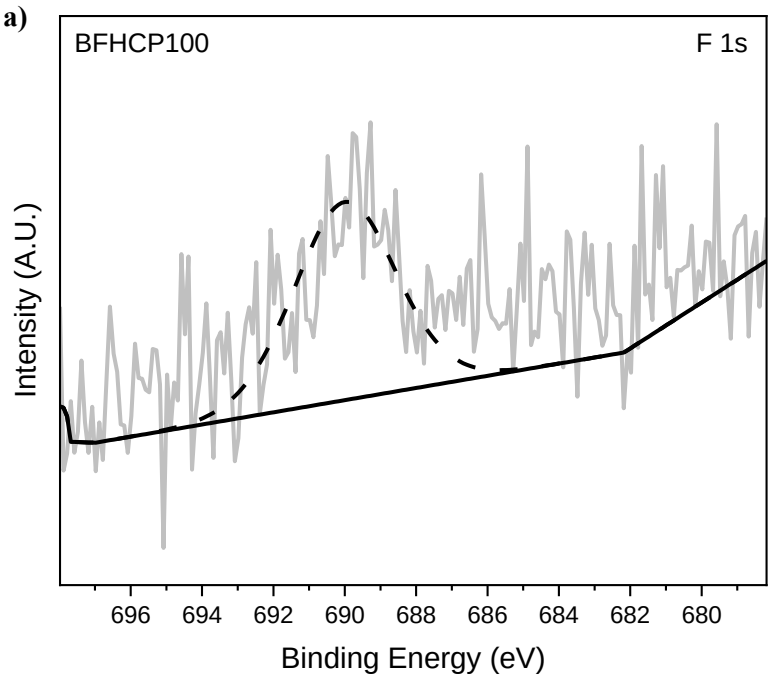
a)
BFHCP100
F 1s
Intensity (A.U.)
696
694
692
690
688
686
684
682
680
Binding Energy (eV)

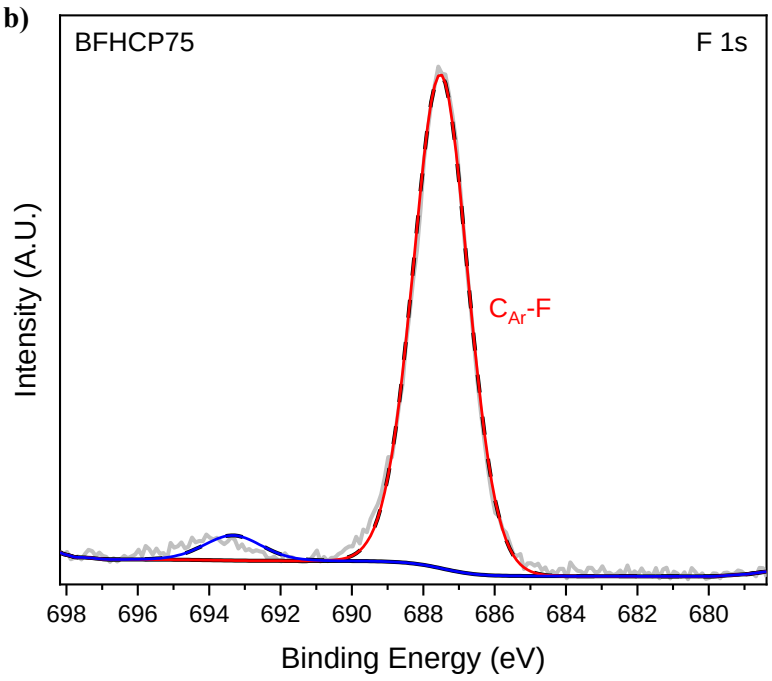
b)
BFHCP75
F 1s
Intensity (A.U.)
C_{Ar}-F
698
696
694
692
690
688
686
684
682
680
Binding Energy (eV)

c)

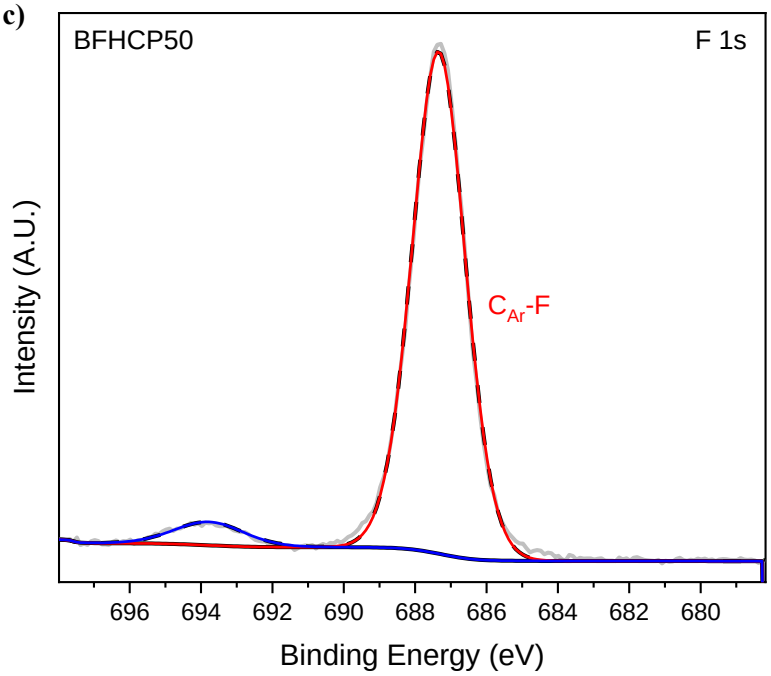
BFHCP50
F 1s
Intensity (A.U.)
C_{Ar}-F
696
694
692
690
688
686
684
682
680
Binding Energy (eV)

d)

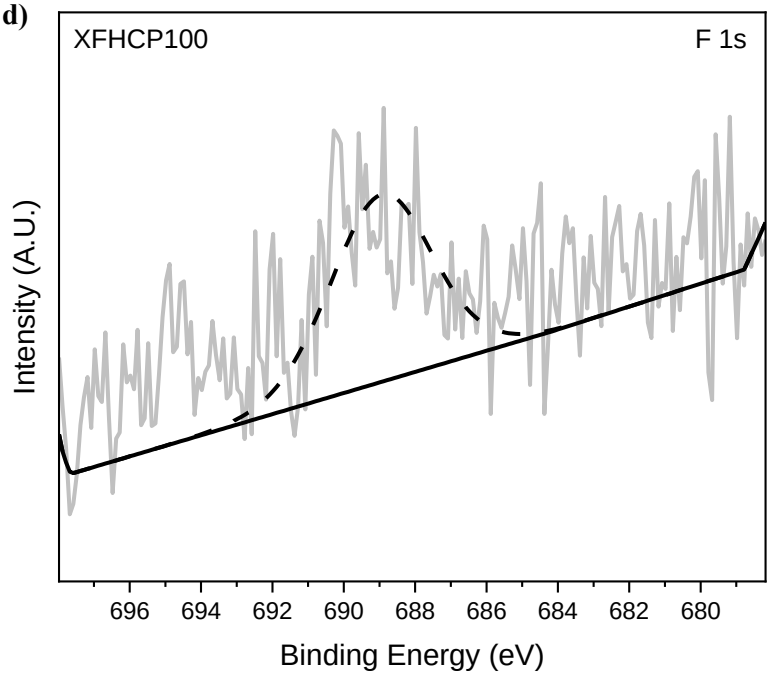
XFHCP100
F 1s
Intensity (A.U.)
696
694
692
690
688
686
684
682
680
Binding Energy (eV)

e)

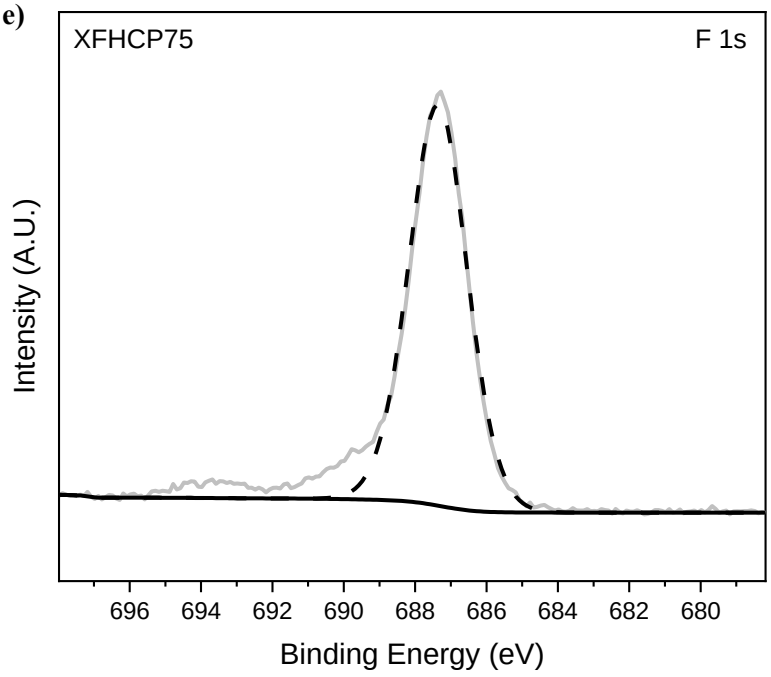
XFHCP75
F 1s
Intensity (A.U.)
696
694
692
690
688
686
684
682
680
Binding Energy (eV)

f)

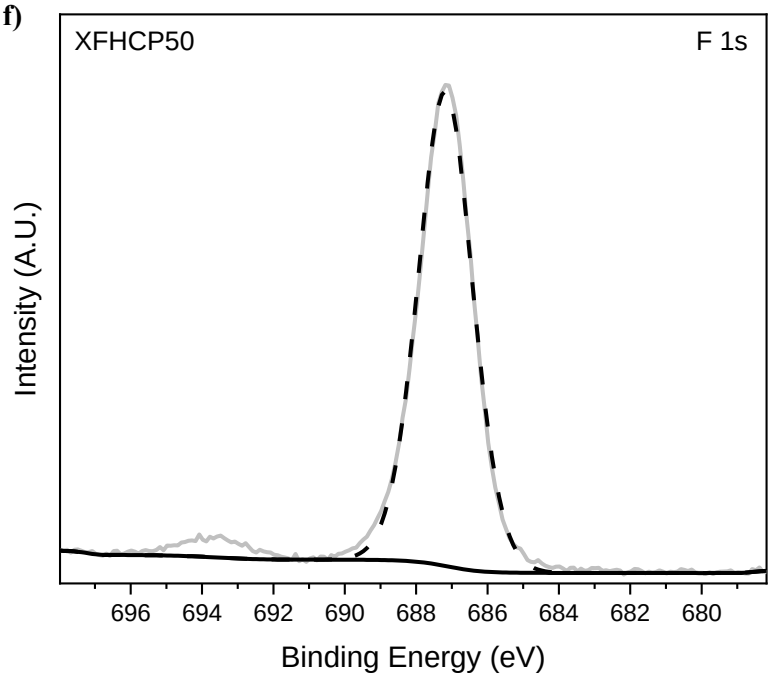
XFHCP50
F 1s
Intensity (A.U.)
696
694
692
690
688
686
684
682
680
Binding Energy (eV)

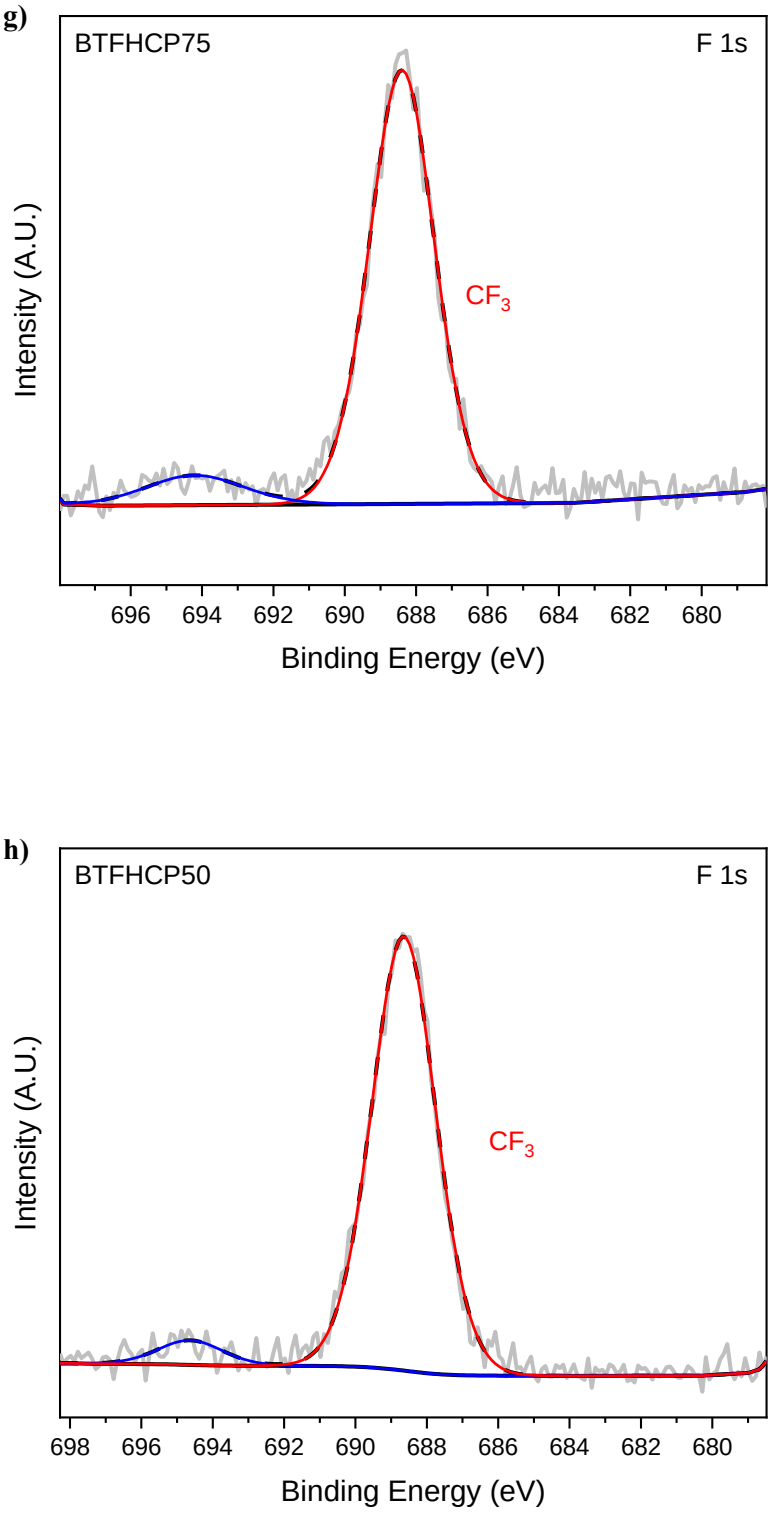

Figure 5. XPS F 1s regions of (a) BFHCP100, (b) BFHCP75, (c) BFHCP50, (d) XFHCP100, (e) XFHCP75, (f) XFHCP50, (g) BTFHCP75 and (h) BTFHCP50.

C 1s peaks in all HCPs were deconvoluted into three peaks ~ 284.9 eV, 287.1 eV and 291.4 eV, which were assigned to C_{Ar}, the combination of C=O, C-Cl and C_{Ar}-F, and C π→π* transition (Figure 6a to 6h) [95], respectively. Unfortunately, CF_3 at 293.1 eV [95] could not be detected in the C1s regions, likely due to the low fluorine contents in BTFHCP75 and BTFHCP50.

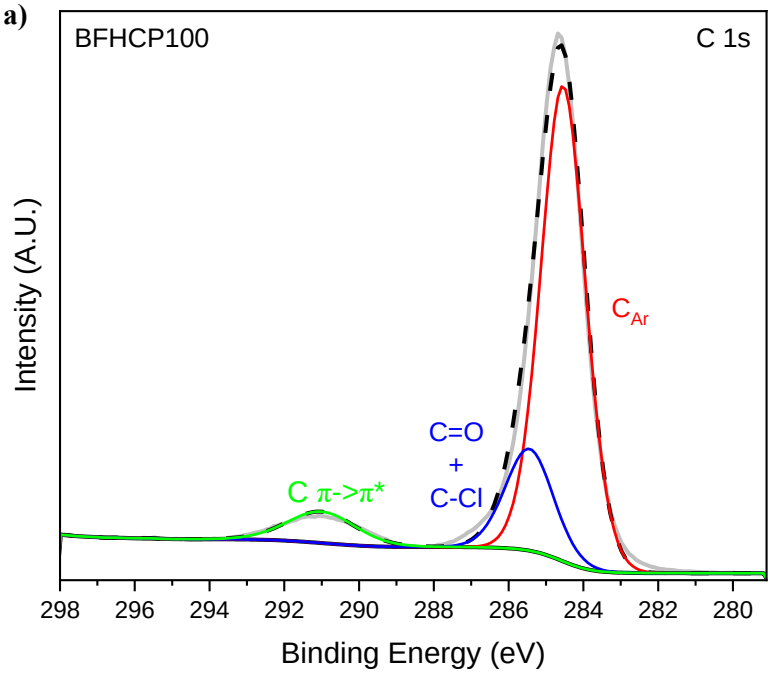

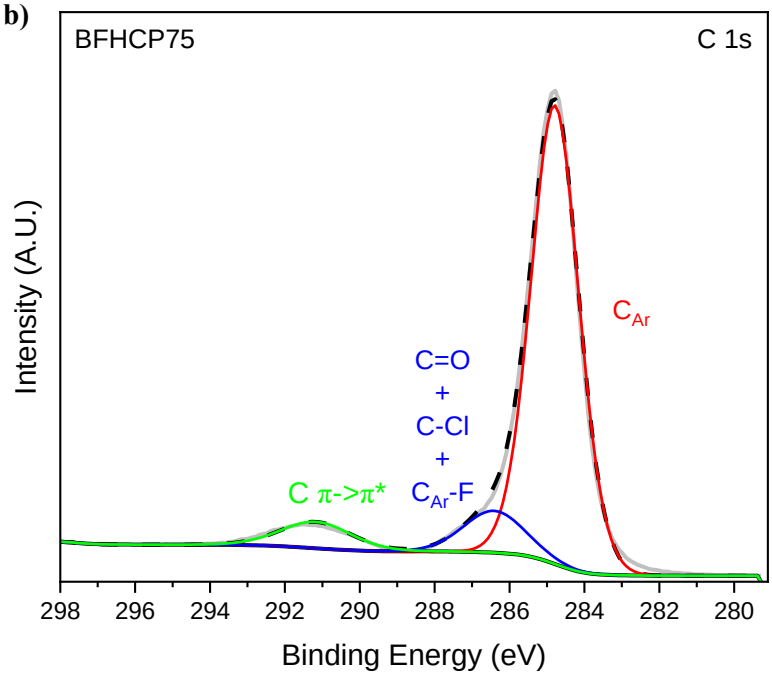

c)

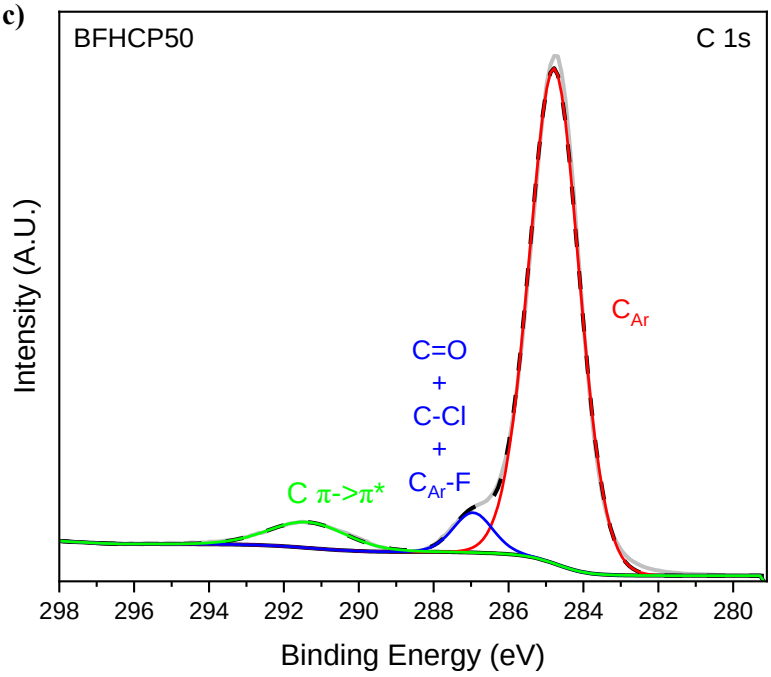
BFHCP50
C 1s
Intensity (A.U.)
C=O
+
C-Cl
+
C$_{Ar}$-F
C$_{Ar}$
C π->π*
298
296
294
292
290
288
286
284
282
280
Binding Energy (eV)

d)

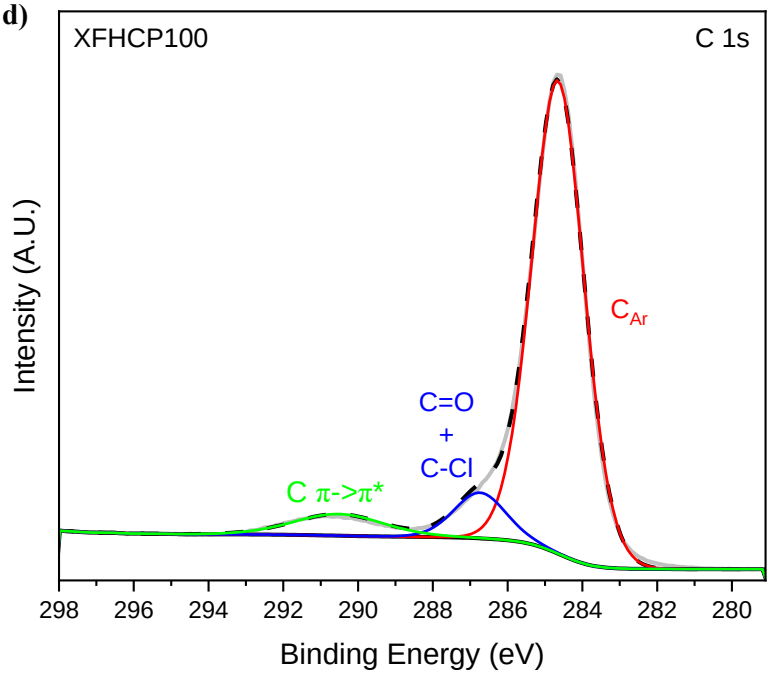
XFHCP100
C 1s
Intensity (A.U.)
C=O
+
C-Cl
C$_{Ar}$
C π->π*
298
296
294
292
290
288
286
284
282
280
Binding Energy (eV)

e)

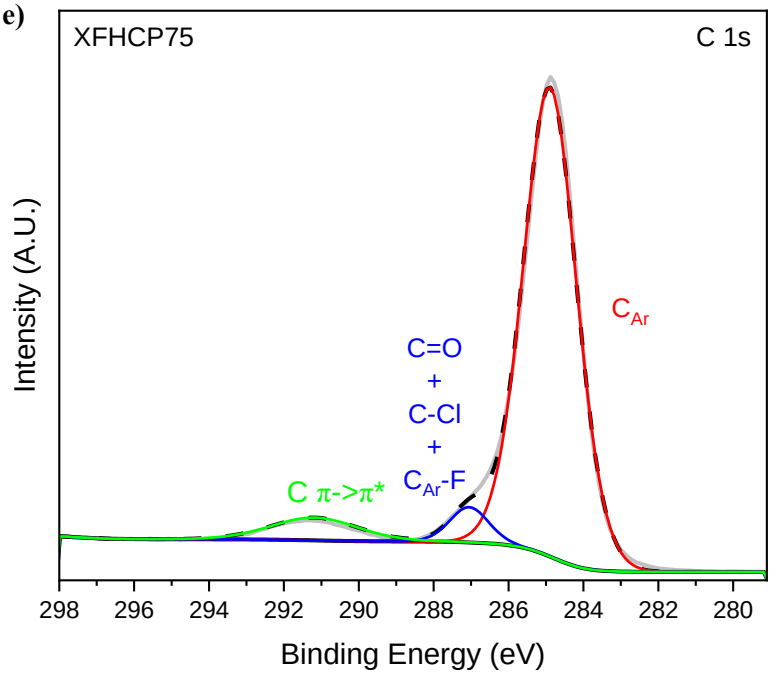
XFHCP75
C 1s
Intensity (A.U.)
C=O
+
C-Cl
+
C_Ar-F
C_Ar
C π->π*
298
296
294
292
290
288
286
284
282
280
Binding Energy (eV)

f)

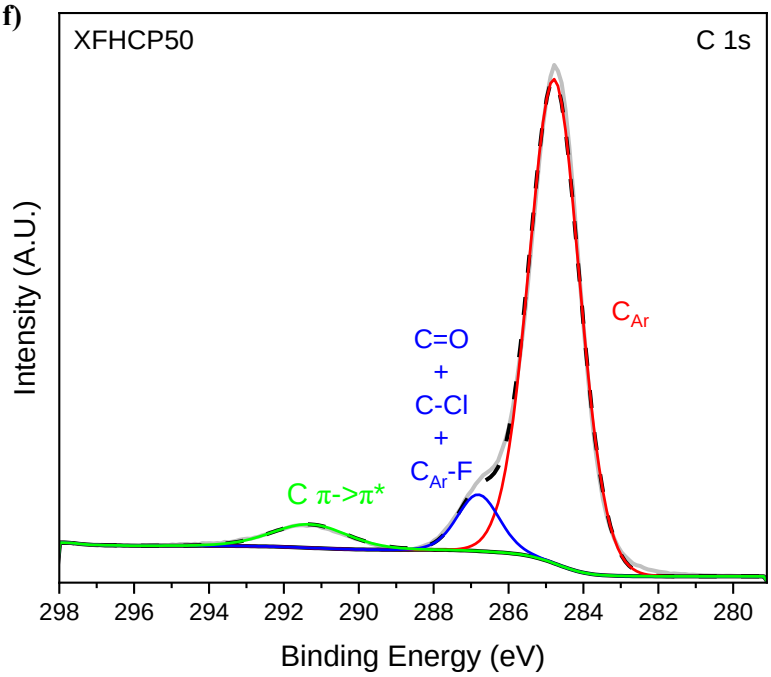
XFHCP50
C 1s
Intensity (A.U.)
C=O
+
C-Cl
+
C_Ar-F
C_Ar
C π->π*
298
296
294
292
290
288
286
284
282
280
Binding Energy (eV)

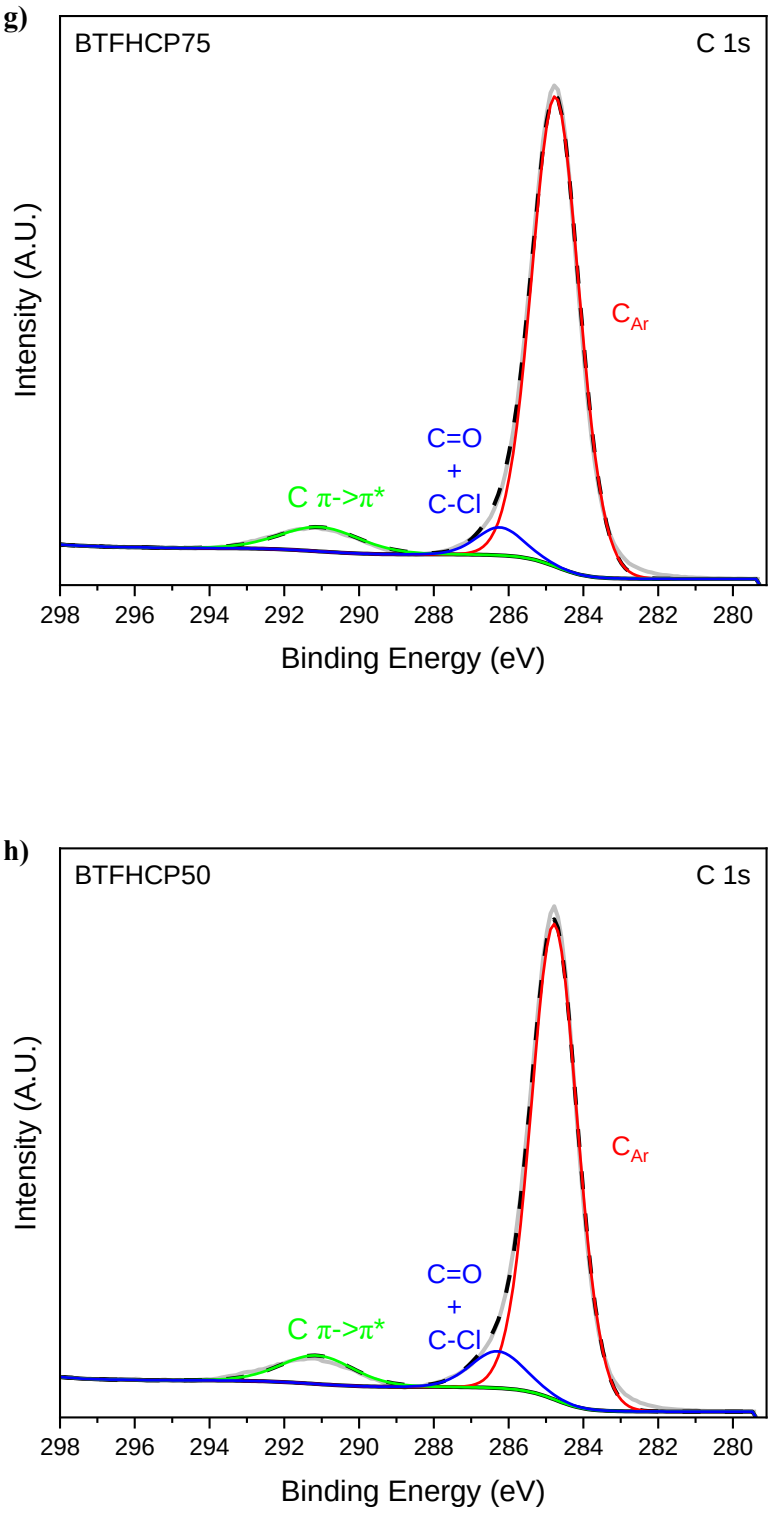

Figure 6. XPS C 1s regions of (a) BFHCP100, (b) BFHCP75, (c) BFHCP50, (d) XFHCP100, (e) XFHCP75, (f) XFHCP50, (g) BTFHCP75 and (h) BTFHCP50.

3.2.4. Porous properties of HCPs

The N_2 adsorption–desorption isotherms were measured at −196 °C. All BFHCP series displayed a combination of type I isotherm and type IV isotherm (Figure 7a) according to the IUPAC classification [72]. Type I isotherms are characteristic of microporous materials having relatively small external surfaces, indicated by the steep uptake in low P/P_0 due to the enhanced adsorbent-adsorbate interactions in the narrow micropores, resulting in micropore filling at low P/P_0. The type IV character indicates mesoporosity, revealed by the hysteresis loop in the desorption path in medium and high P/P_0 associated with capillary condensation. The micro/mesoporosity of the BFHCP series was further confirmed by their PSDs, calculated using QSDFT (Figure 8a). The BET-specific surface areas of the BFHCP series decreased from 1748 ± 78 to 960 ± 114 m^2/g with the increasing pFBC monomer ratio (Table 3), and all total pore volumes, micropore volumes and mesopore volumes displayed similar trends with rising pFBC monomer ratio (Table 3), from 2.85 to 1.66 cm^3/g, 1.40 to 0.99 cm^3/g and 1.45 to 0.67 cm^3/g, respectively, when comparing BFHCP100 and BFHCP50.

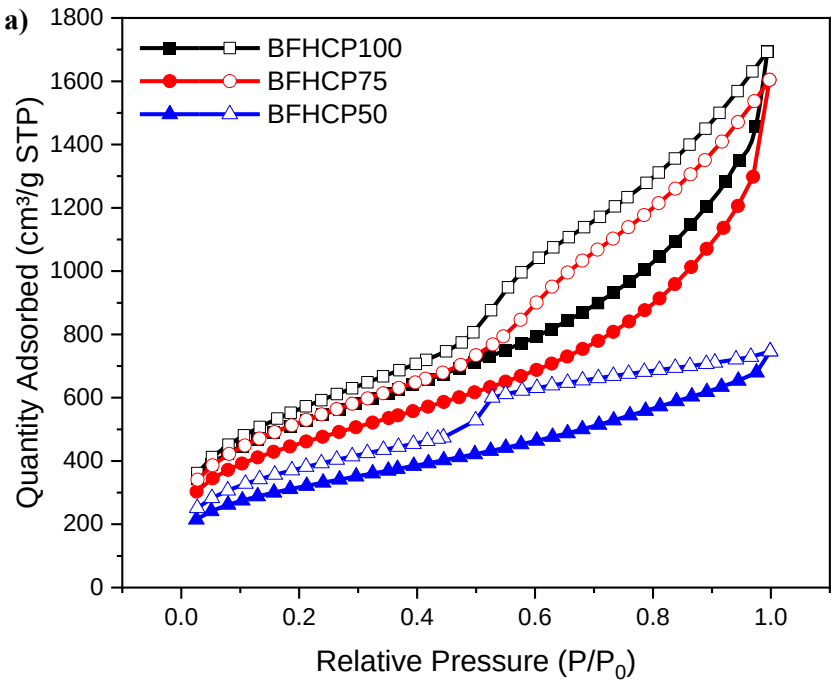

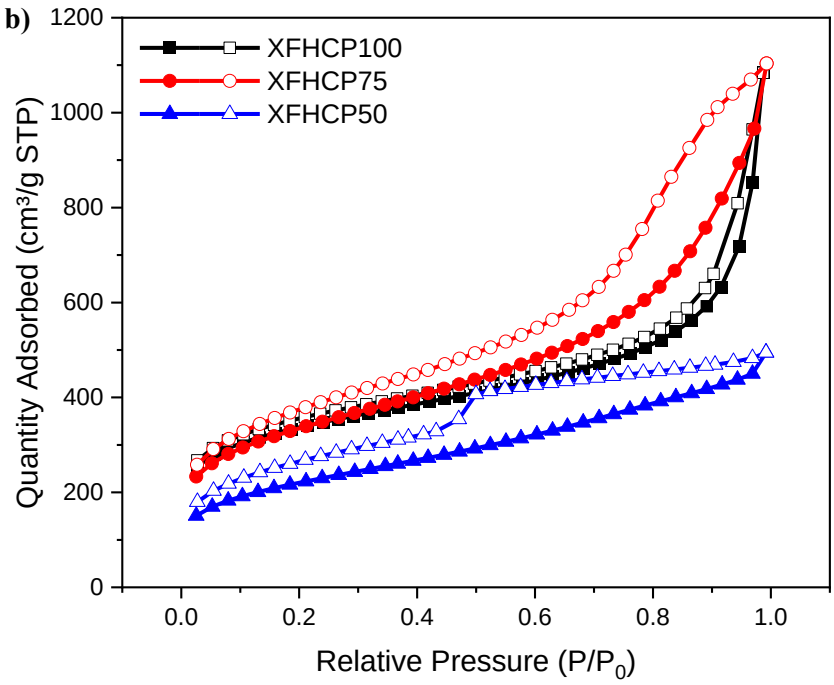

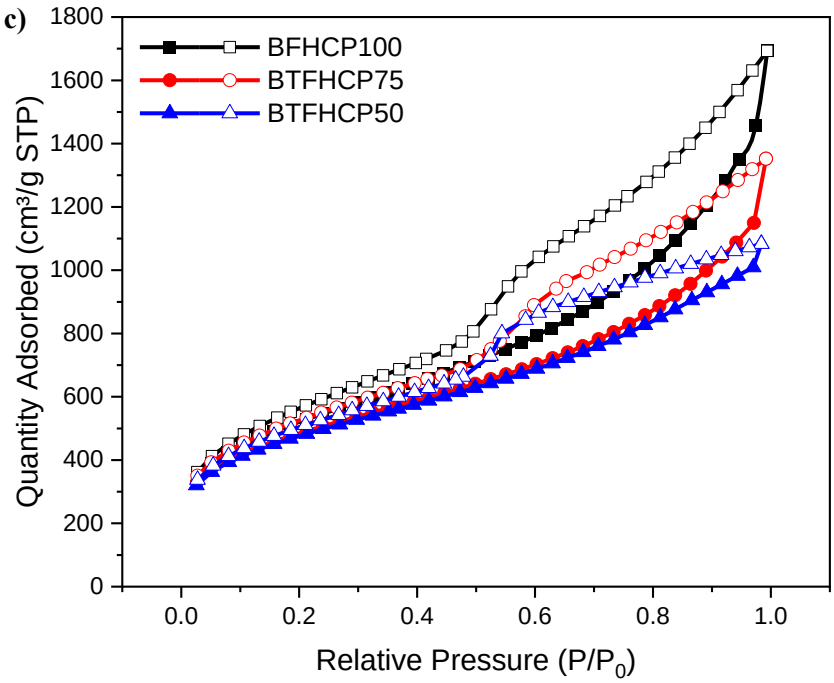

Figure 7. N_2 adsorption-desorption isotherms of (a) BFHCP series, (b) XFHCP series and (c) BTFHCP series.

The XFHCP series displayed similar isotherms (Figure 7b) to the BFHCP series, combining type I and type IV and having typical micro/mesoporosity. XFHCP100 showed a lower mesoporosity than XFHCP75, indicated by the steep and narrow hysteresis loop, reflecting an increase of SSA_{BET} from 1089 ± 105 m^2/g and V_{Mes} from 0.61 cm^3/g for XFHCP100 to 1140 ± 94 m^2/g and 0.84 cm^3/g for XFHCP75, dropping to 691 ± 69 m^2/g and 0.41 cm^3/g for XFHCP50. Moreover, micropores contributed the majority of total pore volume across the XFHCP series (Figure 8b and Table 3).

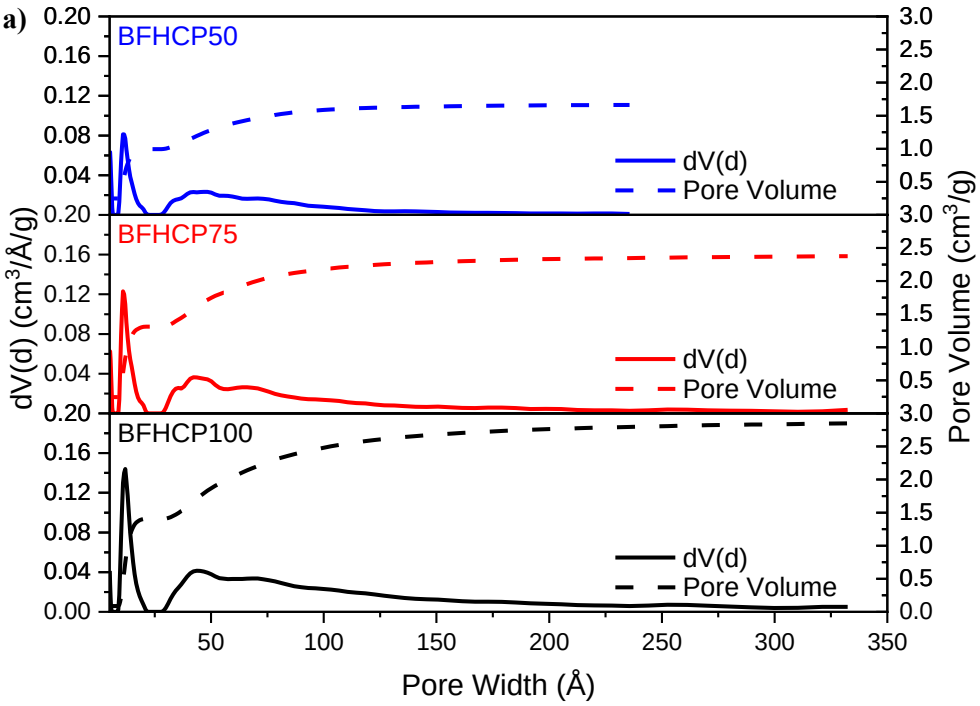

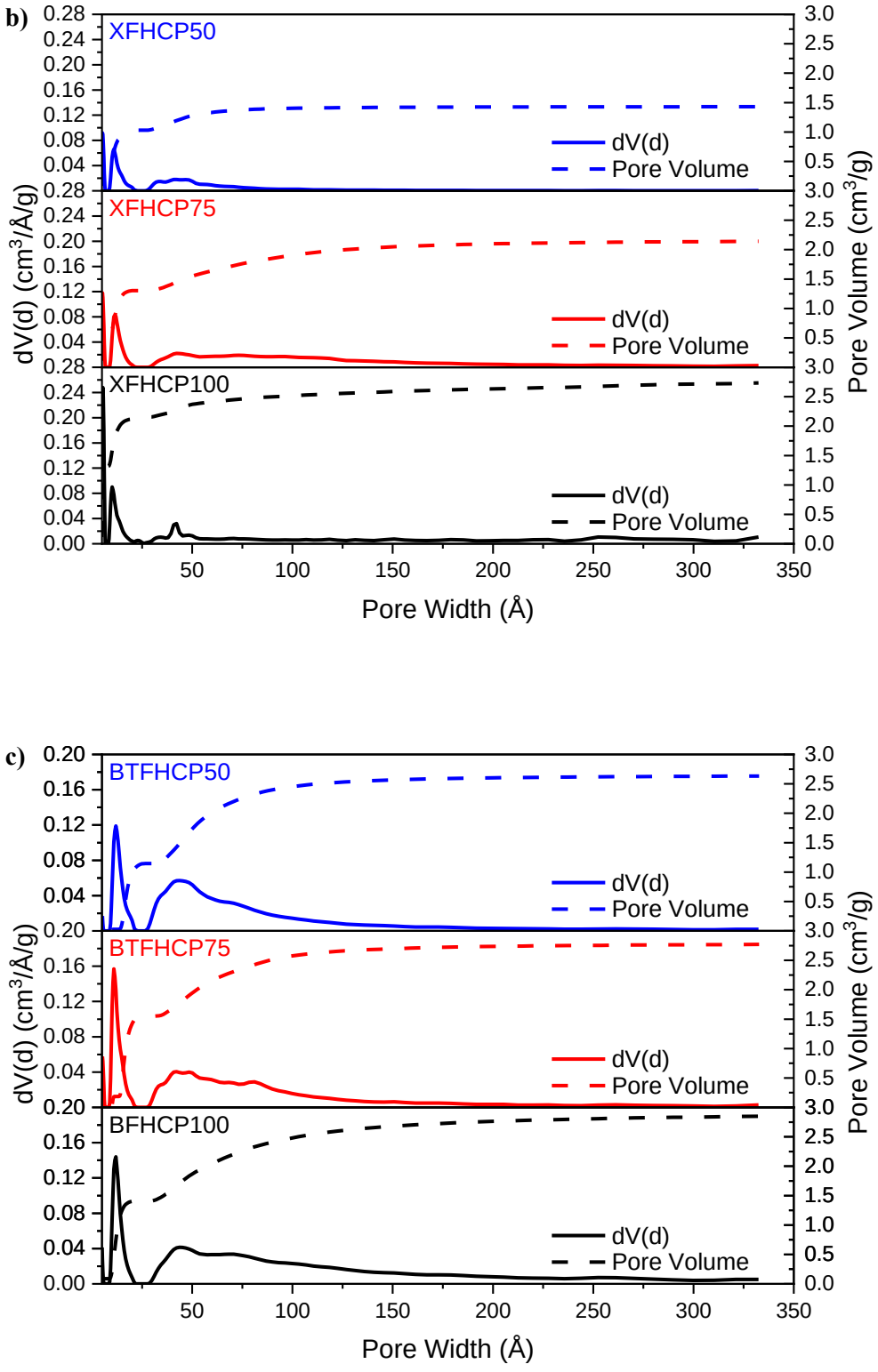

Figure 8. PSDs and cumulative pore volumes of (a) BFHCP series, (b) XFHCP series and (c) BTFHCP series, calculated using QSDFT.

The BTFHCP series also displayed a combination of type I and type IV isotherms (Figure 7c), micro/mesoporosity, and similar PSDs (Figure 8c) compared to the BFHCP series. BTFHCP75 and BTFHCP50 possessed almost the same porous properties, with BTFHCP75 showing SSA_{BET} 1632 ± 31 m^2/g, V_P 2.67 ± 0.15 cm^3/g, V_{Mic} 1.22 ± 0.46 cm^3/g and V_{Mes} 1.45 ± 0.31 cm^3/g, and BTFHCP50 possessing SSA_{BET} 1647 ± 29 m^2/g, V_P 2.67 ± 0.05 cm^3/g, V_{Mic} 1.05 ± 0.11 cm^3/g and V_{Mes} 1.62 ± 0.16 cm^3/g (Table 3). With the exception of V_{Mes}, the porous parameters of both fluorinated HCPs were reduced compared to that of the 4,4'-dimethylbiphenyl framework without BTF.

Table 3. BET-specific surface areas SSA_{BET} and pore volumes of the synthesized HCPs

Series	Sample	SSA_{BET} (m^2/g)	V_P (cm^3/g)	V_{Mic} (cm^3/g)	V_{Mes} (cm^3/g)
BFHCP	BFHCP100	1748 ± 78	2.85	1.40	1.45
	BFHCP75	1403 ± 182	2.38	1.30	1.08
	BFHCP50	960 ± 114	1.66	0.99	0.67
XFHCP	XFHCP100	1089 ± 105	2.73	2.12	0.61
	XFHCP75	1140 ± 94	2.14	1.30	0.84
	XFHCP50	691 ± 69	1.43	1.02	0.41
BTFHCP	BTFHCP75	1632 ± 31	2.67 ± 0.15	1.22 ± 0.46	1.45 ± 0.31
	BTFHCP50	1647 ± 29	2.67 ± 0.05	1.05 ± 0.11	1.62 ± 0.16

3.3. Oil adsorption performance and oil/water separation performance of synthesized HCPs

In this work, we selected toluene, methanol, n-heptane and DCE as typical of aromatic hydrocarbons, alcohols, flexible long straight-chain hydrocarbons and halides, respectively, to assess the adsorption performance of HCPs toward organic solvents. Samples were suspended in solvent and stirred for sufficient time before the solvent was removed via vacuum filtration. The filtered HCP was weighed as soon as possible to minimise losses due to evaporation and finally weighed again after complete drying. More details about the measurement can be found in the Experimental Section. The adsorption capacity was calculated via two methods; the first, k_B, considers the weight of sample before adsorption, as reported in references [38, 54, 61-63, 67]. However, the powdery HCPs in this work, instead of sponge [61, 63], monolithic [62, 67] or magnetic powdery products [38, 54] in literature, had to be removed from solvents via vacuum filtration after oil-adsorption or separation experiment. The error caused by the weight loss during vacuum filtration led to a lower result, hence, the second capacity, k_D, corrected from k_B, was calculated based on the weight of sample after drying, avoiding the error and ensuring results are more accurate and meaningful. Comparing the k_D value with its corresponding k_B value (Figure 9a with 10a, Figure 9b with 10b and Figure 9c with 10c, respectively), the former was always only slightly larger than the latter, therefore the k_D values were comparable with the k_B values in references, and in the following, only k_D was used to represent the adsorption capacity.

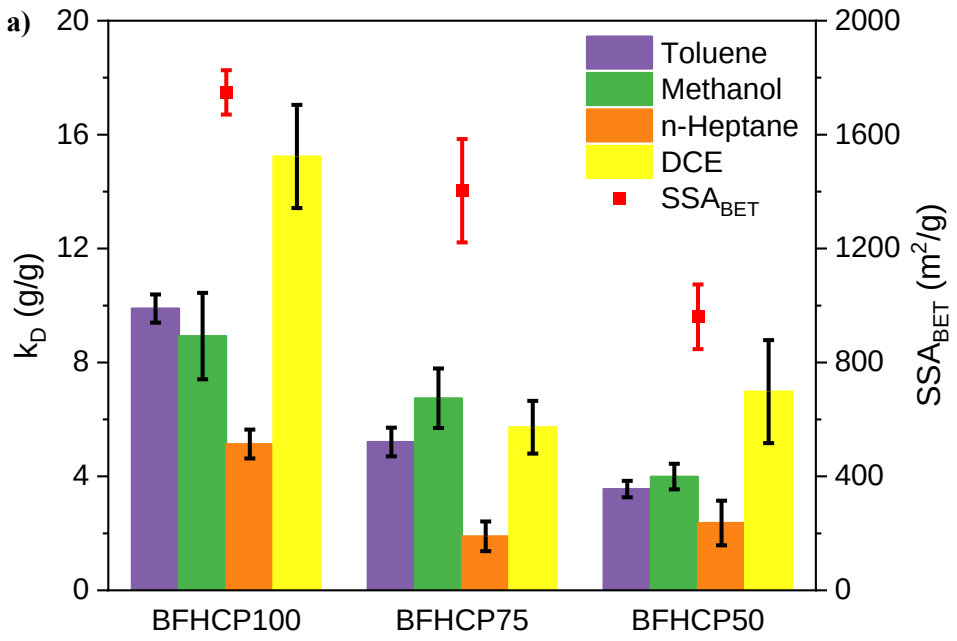
a)
20
16
12
8
4
0
2000
1600
1200
800
400
0
Toluene
Methanol
n-Heptane
DCE
SSA$_{BET}$
k$_D$ (g/g)
SSA$_{BET}$ (m^2/g)
BFHCP100
BFHCP75
BFHCP50

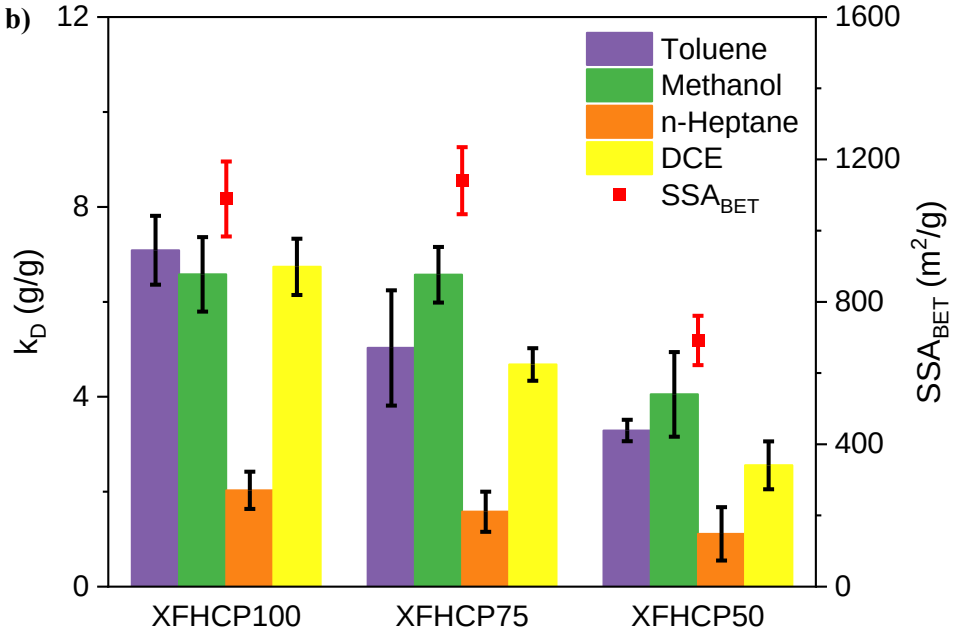
b)
12
8
4
0
1600
1200
800
400
0
Toluene
Methanol
n-Heptane
DCE
SSA$_{BET}$
k$_D$ (g/g)
SSA$_{BET}$ (m^2/g)
XFHCP100
XFHCP75
XFHCP50

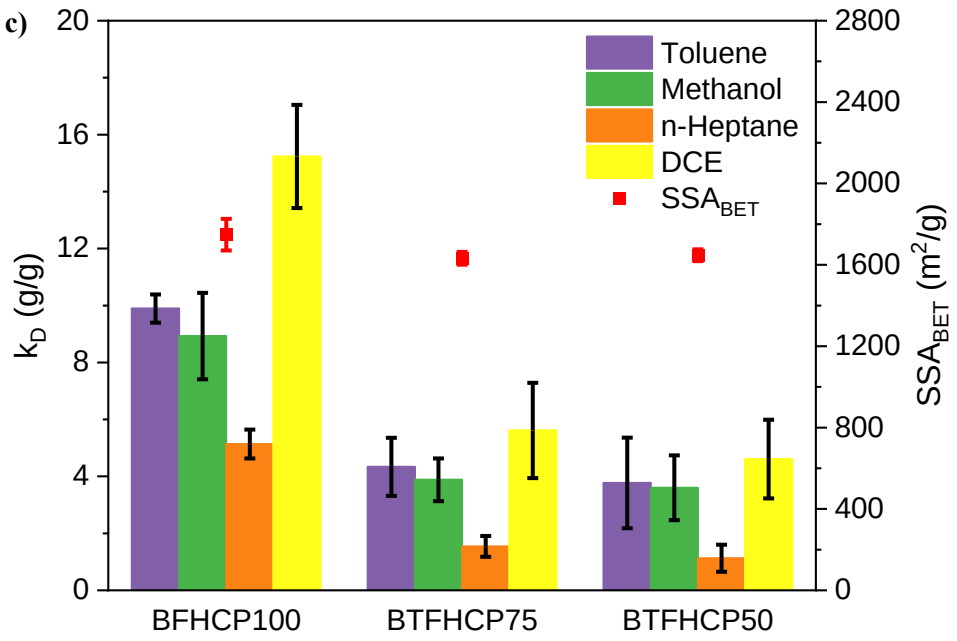

Figure 9. Adsorption capacities k_D of (a) BFHCP series, (b) XFHCP series and (c) BTFHCP series toward different organic solvents, compared to their BET-specific surface areas.

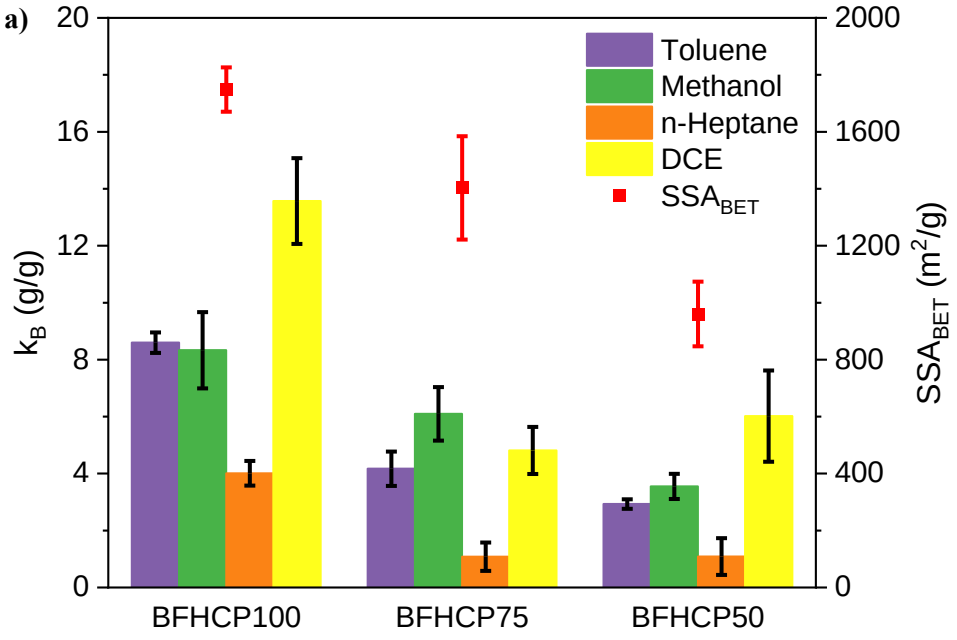

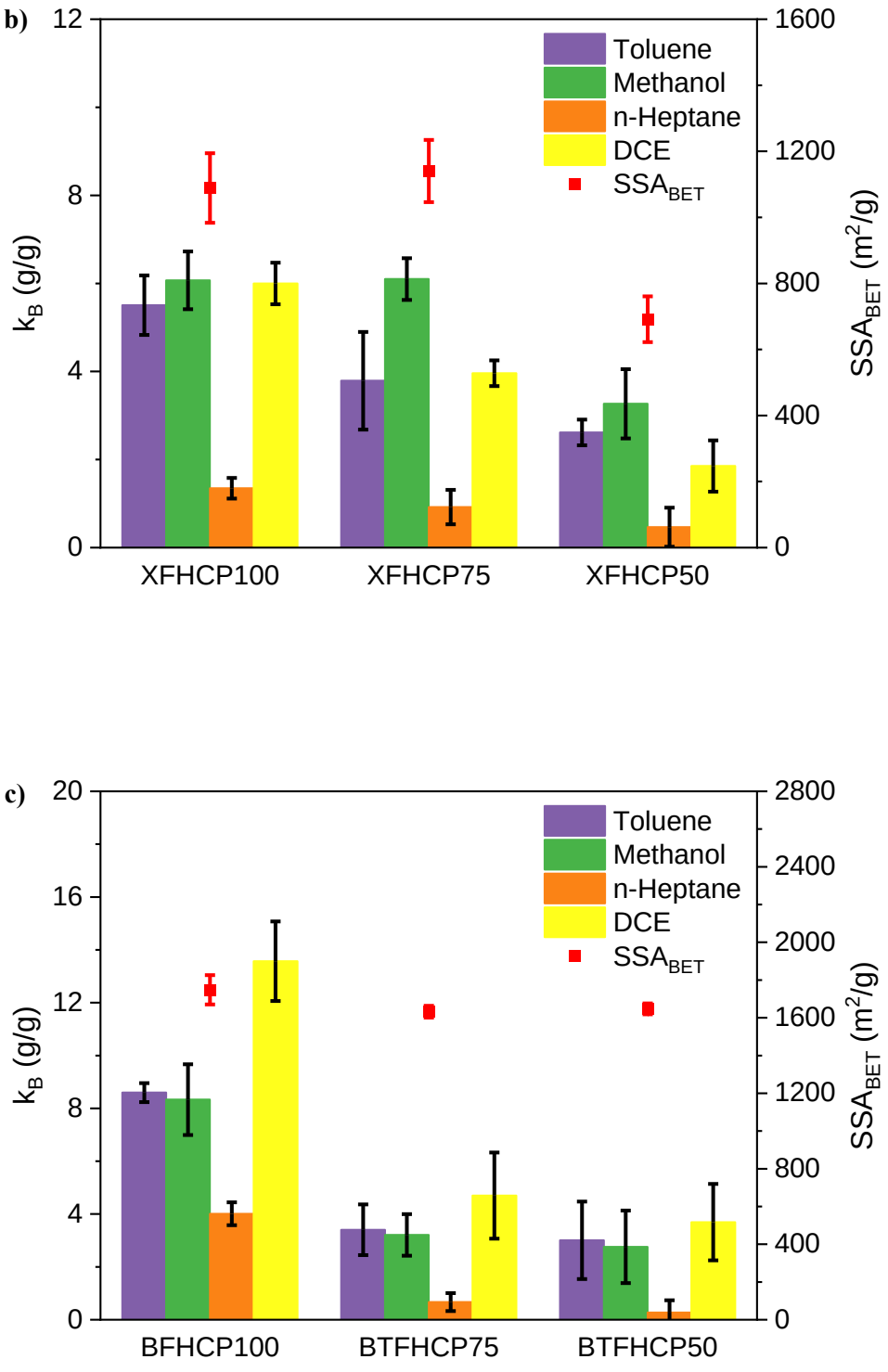

Figure 10. Adsorption capacities k_B of (a) BFHCP series, (b) XFHCP series and (c) BTFHCP series toward different organic solvents, compared to their BET-specific surface areas.

The capacity trend in each series was compared with their SSA_{BET} (Figure 9a to 9c) and V_P (Figure 11a to 11c). Among the BFHCP series, the adsorption capacities of the samples toward both toluene and methanol decreased with their SSA_{BET} (Figure 9a) and V_P (Figure 11a), from 9.89 ± 0.49 to 3.55 ± 0.29 g/g and from 8.92 ± 1.52 to 3.99 ± 0.45 g/g, respectively, when comparing BFHCP100 and BFHCP50. However, the lowest k_D values toward both n-heptane and DCE were observed in BFHCP75, namely 1.90 ± 0.52 and 5.73 ± 0.93 g/g, respectively, not in agreement with SSA_{BET} nor V_P trends. The higher fluorine contents in BFHCP50 could result in its higher adsorption toward DCE through halogen bonding, however this effect would not clarify its higher adsorption toward n-heptane. Therefore, the adsorption mechanism in this work needs further study. Among the XFHCP series, the adsorption capacities toward all four solvents decreased over V_P rather than SSA_{BET} (Figure 9b and Figure 11b), from 7.09 ± 0.73 to 3.29 ± 0.23 g/g toward toluene, from 6.58 ± 0.78 to 4.05 ± 0.89 g/g toward methanol, from 2.03 ± 0.39 to 1.11 ± 0.56 g/g toward n-heptane and from 6.74 ± 0.59 to 2.56 ± 0.50 g/g toward DCE. Among the BTFHCP series, BTFHCP75 and BTFHCP50 exhibited almost the same adsorption capacities toward toluene, methanol, n-heptane and DCE, with almost the same SSA_{BET} (Figure 9c) and V_P (Figure 11c), however, both were smaller than half of those in BFHCP100.

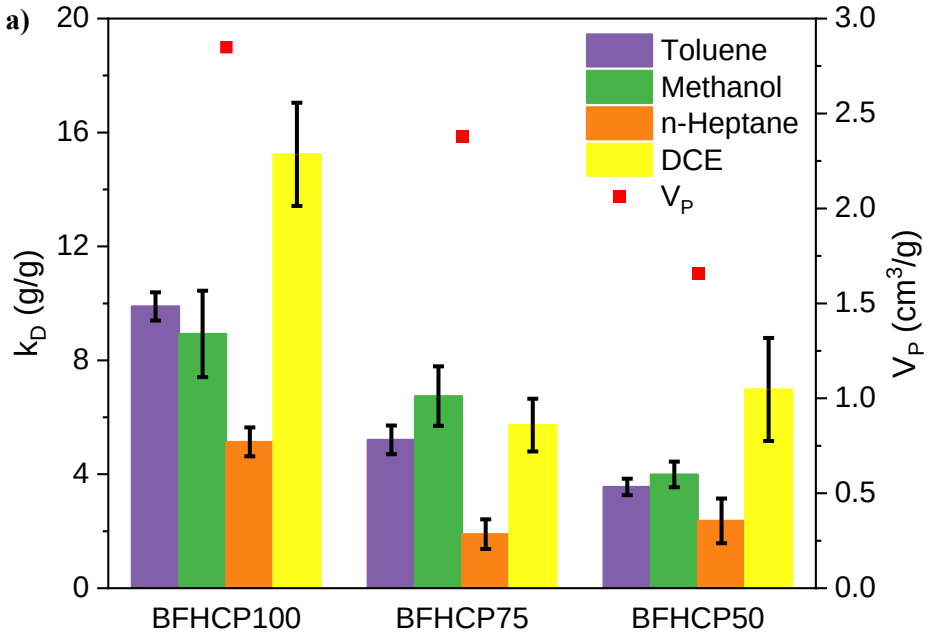

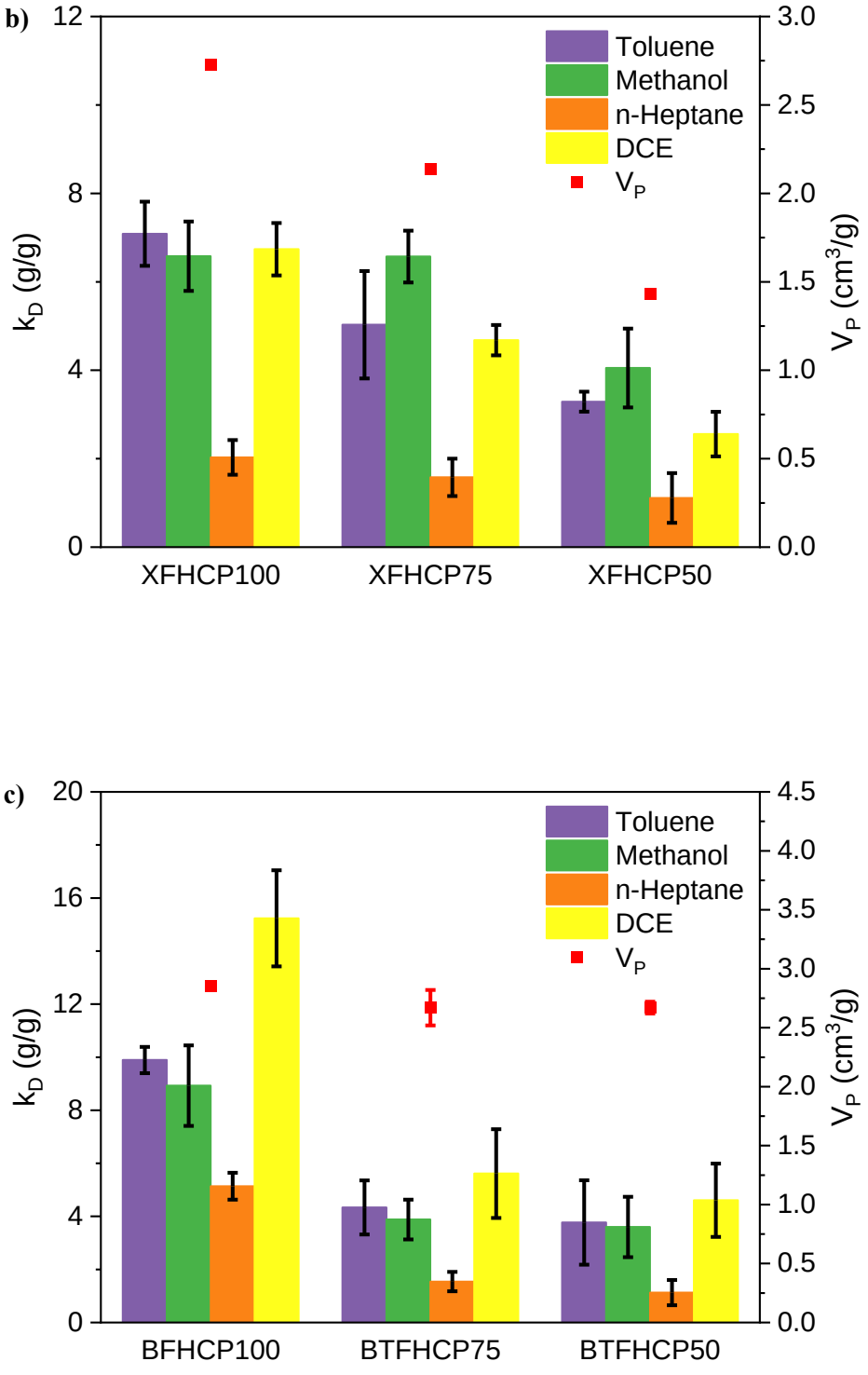

Figure 11. Adsorption capacities k_D of (a) BFHCP series, (b) XFHCP series and (c) BTFHCP series toward different organic solvents, compared to their total pore volumes V_P.

The adsorption performance of synthesized HCPs in this work can be briefly summarized as follows:

1. the adsorption capacities essentially decreased with decreasing V_P, rather than SSA_{BET}, in each series, indicating that the adsorption performance of the HCPs toward organic solvents, including halides, did not benefit from the introduction of fluorine containing monomer, but was instead more dependent on their porous properties;
2. BFHCP100 displayed the highest capacities toward all the four solvents among all product in this work, as well as an excellent adsorption performance comparing with other powdery or particulate adsorbents reported in references (Table 4);
3. the adsorption capacities toward n-heptane were consistently the lowest in each sample, probably due to steric hinderance caused by the large molecule adsorbate.

Table 4. Comparison of adsorption capacities of HCPs reported here with the powdery or particulate oil adsorbents in the literature

Adsorbent[a]	Organic adsorbate	Adsorption capacity (g/g)	Reference
Polystyrene grafted Fe_3O_4 nanosphere	N-hexane	2.90	[96]
Vinyltrimethoxysilane modified rough magnetic silica nanocomposite particle	Methanol Hexane	5.45 3.52	[54]
With ethyl acetate as porogenic solvent synthesized porous poly(divinylbenzene)	Hexane Toluene	12.9 14.1	[68]
Magnetic coco peat powder	Toluene Chloroform Cyclohexane	5.66 8.57 5.12	[38]
Lauric acid modified Douglas fir biochar	Crude oil (from deionized water)	10.6	[37]
With water and ethanol explosion puffed starch	Chili oil	1.41	[97]
Via emulsification technique synthesized silica aerogel microsphere	Isopropanol Hexane	8.16 6.06	[98]
Trichloromethylsilane modified silica aerogel particle	Silicone oil	2.50	[55]
Hexamethyldisilazane modified and supercritical CO_2 dried hydrophobic silica aerogel microsphere	Vacuum pump oil Colza oil Hexane	18.9 18.3 11.8	[53]
Fluorinated polydivinylbenzene powder	Toluene Dichloromethane Hexane Trifluoroethanol	0.94 3.60 1.06 1.96	[83]
BFHCP100	Toluene Methanol N-heptane DCE	9.89 8.92 5.13 15.23	This work

[a] Only the adsorbent exhibiting the best adsorption performance in each reference was listed.

The adsorption capacity k_D of BFHCP100 and BFHCP75 toward distilled water was also determined, displaying 7.89 ± 0.52 and 1.36 ± 0.23 g/g (Figure 12), respectively. The water adsorption performance of BFHCP75 was significantly lower than that of BFHCP100, caused by the combination of a reduction in SSA_{BET} and V_P, as well as the hydrophobicity of the introduced p-fluorobenzyl group, reducing water influx to the HCPs' pores [37, 79]. Better oil/water selectivity may result in better separation efficiency, thus we selected BFHCP100 and BFHCP75 as the adsorbents to test their oil/water separation

performance in the removal of toluene from distilled water.

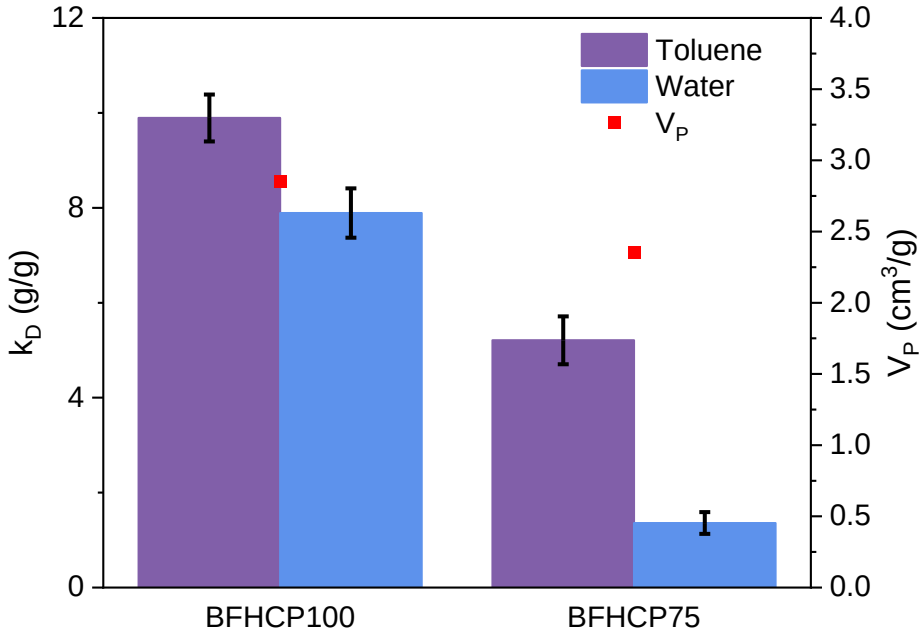

Figure 12. Adsorption capacities k_D of BFHCP100 and BFHCP75 toward toluene and water, compared to their total pore volumes V_P.

Sudan III dye was added to toluene at a concentration of 0.01 g/mL to allow better visualization of the separation process. The oil/water mixture was prepared with the volume ratio $V_{toluene}$:V_{water} = 1:40 in a 25 mL measuring cylinder to simulate a small amount of organic pollutants floating on a water surface. As shown in Figure 13, Sudan III dyed toluene was successfully adsorbed and removed from the water using both BFHCP100 and BFHCP75, demonstrating their practicality as oil adsorbent in actual oil/water separation. The adsorption efficiencies AE of BFHCP100 and BFHCP75 reached up to 90.25% and 95.11%, respectively, revealing that both samples selectively adsorbed toluene in the separation process.

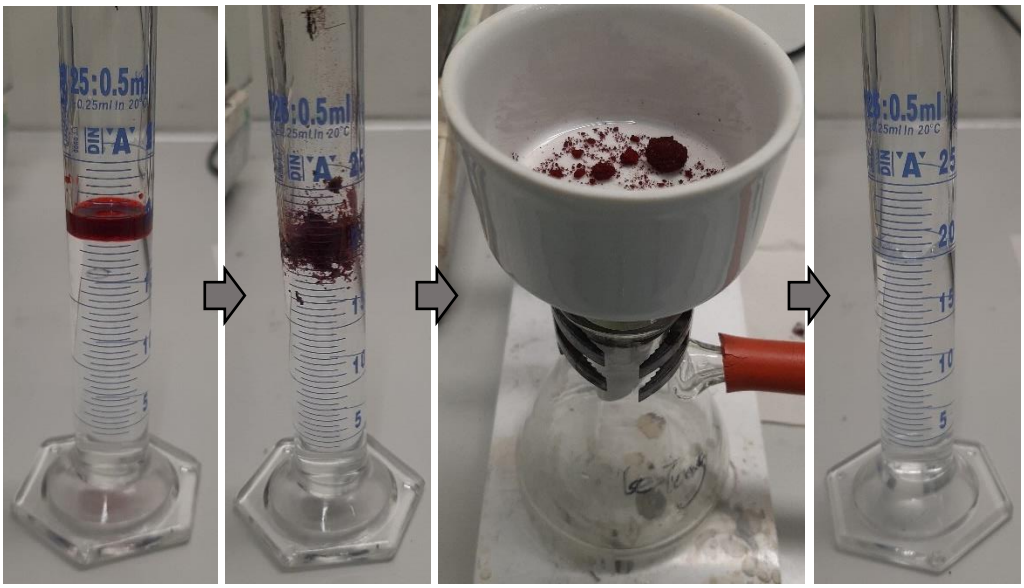

Figure 13. Removal process of Sudan III dyed toluene from water using BFHCP75.

The separation efficiencies SE of BFHCP100 and BFHCP75 were measured via the weight difference of the aqueous phase before and after separation, both displaying 96% (Figure 14). In a control experiment, 20 mL of water alone was put through the same process to determine the water loss due to vacuum filtration. The actual separation efficiencies SE_a of both samples were calculated as follows:

$$SE_a = 100\% - SE_c + SE_m \quad (7)$$

where SE_c and SE_m were the measured separation efficiencies of control and both samples, respectively. After removing the influence of vacuum filtration, the actual separation efficiencies of BFHCP100 and BFHCP75 reached up to 99.5 ± 0.4 % and 99.4 ± 0.4 %, respectively, both achieving efficient separation. The large difference in oil/water selectivity between BFHCP100 and BFHCP75 did not result in a significant difference in their SE, likely due to different conditions in adsorption capacity measurements and separation experiments. The former was determined over 1 h with more vigorous stirring (250 rpm) to obtain maximal values, while the latter was achieved in several seconds with only gentle agitation (by hand).

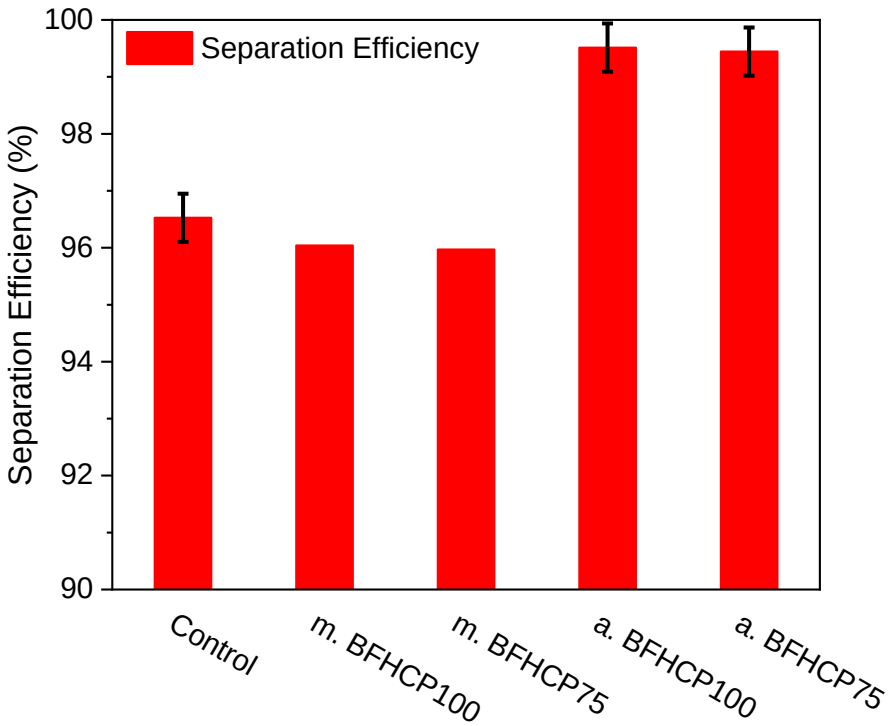

Figure 14. Measured separation efficiencies of control, BFHCP100 and BFHCP75, and actual separation efficiencies of BFHCP100 and BFHCP75, wherein m. represents measured and a. represents actual.

3.4. Resistance of synthesized HCPs to organic solvents and water

Finally, the FTIR spectra and SSA_{BET} of all the recycled samples from adsorption as well as the complete N_2 adsorption-desorption isotherms of the recycled samples were measured to investigate the resistance of the HCPs to organic solvents and water, shown with BFHCP75 as an example. The FTIR spectra of BFHCP75 recovered from the adsorption of all four organic solvents and water were almost the same as that of the pristine sample (Figure 15), indicating no measurable change of functional groups in infrared spectra after separation, recovery and drying.

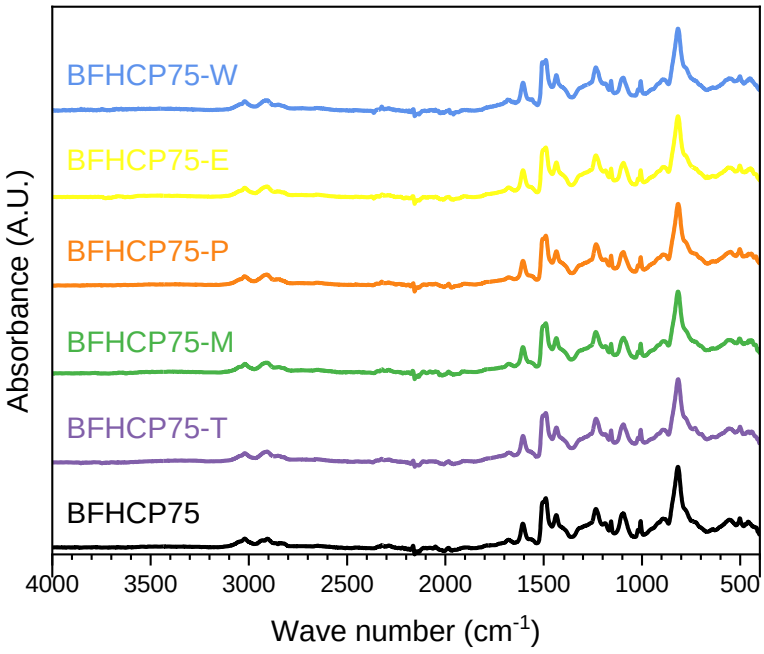

Figure 15. Comparison of the FTIR spectra of the pristine BFHCP75 and BFHCP75 recovered from the adsorption of organic solvents and water, wherein T represents the samples recovered from the adsorption of toluene, M represents those of methanol, P represents those of n-heptane, E represents those of DCE and W represents those of water.

Moreover, the N_2 adsorption isotherms of the recycled BFHCP75 from the adsorption of DCE and water displayed a slight reduction in the mesopore region compared to the pristine samples (Figure 16), resulting in the decreasing of its SSA_{BET} from 1568 to 1536 and 1531 m^2/g, respectively. Similar slight decreases in SSA_{BET} were observed in the recycled BFHCP75 from the adsorption of toluene, methanol and n-heptane, to 1296, 1389 and 1363 m^2/g (Table 5), respectively. As shown in Table 5, SSA_{BET} were also reduced slightly in most of the other recycled samples compared to the pristine samples, while they increased slightly in some recycled samples from the adsorption of methanol, such as BFHCP100-M, XFHCP75-M and XFHCP50-M. The swelling/shrinkage of the network during the solvent adsorption/desorption process may lead some changes in pore structures, resulting in the increase or decrease in SSA_{BET}. The reason for the irregularity of the (slight) changes in this work are unclear and may simply be due to measurement errors from insufficient data. Therefore, it is necessary to obtain more data on the changes in SSA_{BET} after adsorption in further research.

The above results demonstrated the excellent resistance of the HCPs in this work to organic solvents and water, favourable for their potential application in the adsorption and recycling of organic pollutants from wastewater.

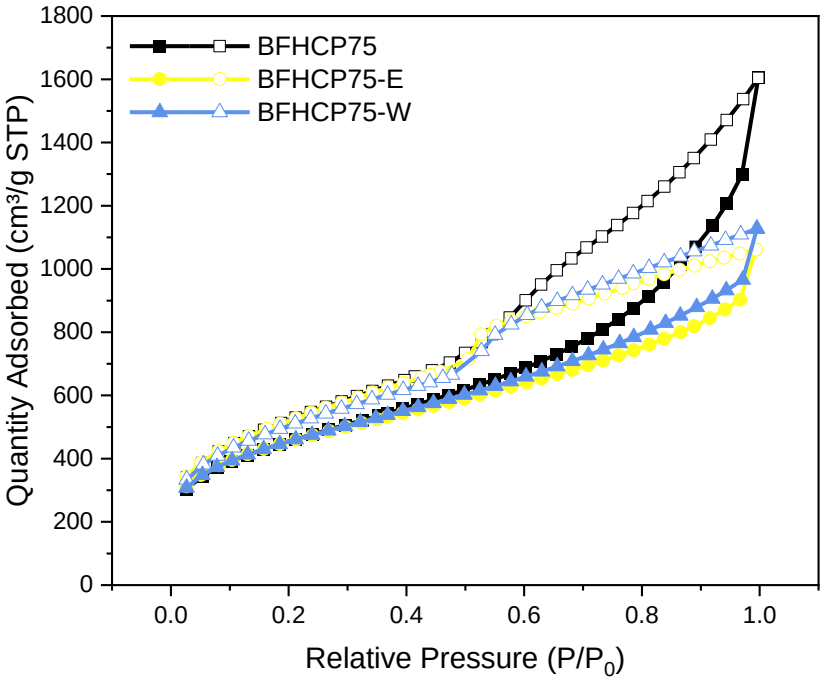

Figure 16. Comparison of the N_2 adsorption-desorption isotherms of the pristine BFHCP75 and BFHCP75 recovered from the adsorption of DCE and water.

Table 5. Comparison of the pristine and recovered HCPs about their SSA_{BET}

a) BFHCP series

Sample	SSA_{BET} (m^2/g)
BFHCP100	1748 ± 78
BFHCP100-M	1848
BFHCP100-E	1740
BFHCP100-W	1722
BFHCP75	1403 ± 182
BFHCP75-T	1296
BFHCP75-M	1389
BFHCP75-P	1362
BFHCP75-E	1371 ± 233
BFHCP75-W	1531
BFHCP50	960 ± 114
BFHCP50-T	844
BFHCP50-M	951
BFHCP50-P	896 ± 87
BFHCP50-E	824 ± 88

b) XFHCP series

Samples	SSA_{BET} (m^2/g)
XFHCP100	1089 ± 105
XFHCP100-T	1131
XFHCP100-M	1195
XFHCP100-E	1068
XFHCP75	1140 ± 94

XFHCP75-T	1147
XFHCP75-M	1218
XFHCP75-P	1139
XFHCP75-E	1091
XFHCP50	691 ± 69
XFHCP50-T	647
XFHCP50-M	821
XFHCP50-P	670 ± 14
XFHCP50-E	577

c) BTFHCP series

Samples	SSA_{BET} (m^2/g)
BTFHCP75	1632 ± 31
BTFHCP75-T	1506
BTFHCP75-E	1673
BTFHCP50	1647 ± 29
BTFHCP50-T	1627 ± 33

4. Conclusions

In summary, various fluorinated HCPs synthesized from BCMBP or pDCX, as framework formation monomer, as well as pFBC or BTF, as fluorine-containing monomer with different monomer ratios were successfully prepared through $FeCl_3$ catalyzed Friedel-Crafts benzylation. The synthesis approach was facile and the generated products exhibited BET-specific surface areas of up to 1748 cm^2/g, high thermal stability and excellent resistance to organic solvents and water. Further, their fluorine contents were controllable by using different fluorine-containing monomer ratios. Among all HCPs prepared in this work, BFHCP100, the product based on the self-condensation of BCMBP, displayed the best oil adsorption performance toward a series of organic solvents (max. 15.23 g/g toward DCE) and achieved efficient oil/water separation of over 99%, possessing potential application as oil adsorbent for the removal of organic pollutants from wastewater. However, the results also indicated that the BET-specific surface area, the oil adsorption performance, and the oil/water separation efficiency of HCPs did not benefit from the inclusion of fluorine.

References

1. Rashed, M.N., *Adsorption technique for the removal of organic pollutants from water and wastewater*, in *Organic pollutants-monitoring, risk and treatment*. 2013. p. 167-194.
2. Ali, I., Asim, M., and Khan, T.A., *Low cost adsorbents for the removal of organic pollutants from wastewater.* Journal of environmental management, 2012. **113**: p. 170-183.
3. Singh, A.K., Kumar, A., and Chandra, R., *Environmental pollutants of paper industry wastewater and their toxic effects on human health and ecosystem.* Bioresource Technology Reports, 2022. **20**: p. 101250.
4. Yusuf, M., Kumar, M., Khan, M.A., Sillanpää, M., and Arafat, H., *A review on exfoliation, characterization, environmental and energy applications of graphene and graphene-based composites.* Advances in colloid and interface science, 2019. **273**: p. 102036.
5. Mukhopadhyay, A., Duttagupta, S., and Mukherjee, A., *Emerging organic contaminants in global community drinking water sources and supply: A review of occurrence, processes and remediation.*

Journal of Environmental Chemical Engineering, 2022. **10**(3): p. 107560.
6. Liu, Y., Lyu, Q., Wang, Z., Sun, Y., Li, C., Sun, S., Lin, L.-C., and Hu, S., *A flame-retardant post-synthetically functionalized COF sponge as absorbent for spilled oil recovery.* Journal of Materials Science, 2021. **56**(23): p. 13031-13042.
7. Singh, P., Rajkhowa, S., and Hussain, C.M., *Impact and Issues of Organic Pollutants.* Management of contaminants of emerging concern (CEC) in environment, 2021: p. 93-126.
8. Hussain, A., Kumari, R., Sachan, S.G., and Sachan, A., *Biological wastewater treatment technology: Advancement and drawbacks*, in *Microbial Ecology of Wastewater Treatment Plants*. 2021, Elsevier. p. 175-192.
9. Girolkar, S., Thawale, P., and Juwarkar, A., *Bacteria-assisted phytoremediation of heavy metals and organic pollutants: Challenges and future prospects.* Bioremediation for environmental sustainability, 2021: p. 247-267.
10. He, Z., Ong, J.H., Bao, Y., and Hu, X., *Chemocatalytic ceramic membranes for removing organic pollutants in wastewater: A review.* Journal of Environmental Chemical Engineering, 2023. **11**(2): p. 109548.
11. Kumar, P.S. and Prasannamedha, G., *Biological and chemical impacts on marine biology.* Modern Treatment Strategies for Marine Pollution; Elsevier: Amsterdam, The Netherlands, 2021: p. 11-27.
12. Schwarzenbach, R.P., Egli, T., Hofstetter, T.B., Von Gunten, U., and Wehrli, B., *Global water pollution and human health.* Annual review of environment and resources, 2010. **35**(1): p. 109-136.
13. Nidheesh, P., *Removal of organic pollutants by peroxicoagulation.* Environmental Chemistry Letters, 2018. **16**(4): p. 1283-1292.
14. DeLuca, S.J., Chao, A.C., and Smallwood Jr, C., *Removal of organic priority pollutants by oxidation-coagulation.* Journal of Environmental Engineering, 1983. **109**(1): p. 36-46.
15. Hao, L., Yan, J., Li, M., Shao, W., and Zeng, M., *Coagulation-centered three-step approach for removing by-product organic pollutants from tetrabromobisphenol A industrial wastewater: Experimental and theoretic investigations.* Environmental Research, 2024. **247**: p. 118113.
16. Adelodun, B., Ogunshina, M.S., Ajibade, F.O., Abdulkadir, T.S., Bakare, H.O., and Choi, K.S., *Kinetic and prediction modeling studies of organic pollutants removal from municipal wastewater using Moringa oleifera biomass as a coagulant.* Water, 2020. **12**(7): p. 2052.
17. Zhu, B., Hu, Y., Kennedy, S., Milne, N., Morris, G., Jin, W., Gray, S., and Duke, M., *Dual function filtration and catalytic breakdown of organic pollutants in wastewater using ozonation with titania and alumina membranes.* Journal of membrane science, 2011. **378**(1-2): p. 61-72.
18. Kim, Y., Osako, M., and Lee, D., *Removal of hydrophobic organic pollutants by coagulation-precipitation process with dissolved humic matter.* Waste management & research, 2002. **20**(4): p. 341-349.
19. Urbano, B.F., Bustamante, S., Palacio, D.A., Vera, M., and Rivas, B.L., *Polymer supports for the removal and degradation of hazardous organic pollutants: an overview.* Polymer International, 2020. **69**(4): p. 333-345.
20. Hassan, M.M. and Carr, C.M., *A critical review on recent advancements of the removal of reactive dyes from dyehouse effluent by ion-exchange adsorbents.* Chemosphere, 2018. **209**: p. 201-219.
21. Garud, R., Kore, S., Kore, V., and Kulkarni, G., *A Short Review on Process and Applications of Reverse Osmosis.* Universal Journal of Environmental Research & Technology, 2011. **1**(3).
22. Wang, J., Wang, Z., Vieira, C.L., Wolfson, J.M., Pingtian, G., and Huang, S., *Review on the treatment of organic pollutants in water by ultrasonic technology.* Ultrasonics sonochemistry, 2019. **55**: p.

273-278.
23. Sancheti, S.V., Saini, C., Ambati, R., and Gogate, P.R., *Synthesis of ultrasound assisted nanostuctured photocatalyst (NiO supported over CeO2) and its application for photocatalytic as well as sonocatalytic dye degradation.* Catalysis Today, 2018. **300**: p. 50-57.
24. Mateescu, C., Lungulescu, E.-M., and Nicula, N.-O., *Effectiveness of Biological Approaches for Removing Persistent Organic Pollutants from Wastewater: A Mini-Review.* Microorganisms, 2024. **12**(8): p. 1632.
25. Hanafi, M.F. and Sapawe, N., *A review on the current techniques and technologies of organic pollutants removal from water/wastewater.* Materials Today: Proceedings, 2020. **31**: p. A158-A165.
26. Lefebvre, O. and Moletta, R., *Treatment of organic pollution in industrial saline wastewater: a literature review.* Water research, 2006. **40**(20): p. 3671-3682.
27. Arulazhagan, P., Vasudevan, N., and Yeom, I., *Biodegradation of polycyclic aromatic hydrocarbon by a halotolerant bacterial consortium isolated from marine environment.* International Journal of Environmental Science & Technology, 2010. **7**: p. 639-652.
28. Kumari, P., Bahadur, N., Cretin, M., Kong, L., O'Dell, L.A., Merenda, A., and Dumée, L.F., *Electro-catalytic membrane reactors for the degradation of organic pollutants–a review.* Reaction Chemistry & Engineering, 2021. **6**(9): p. 1508-1526.
29. Rashed, M.N., *Application of Different Advanced Oxidation Processes for the Degradation of Organic Pollutants*, in *Organic pollutants: monitoring, risk and treatment*. 2013. p. 141-166.
30. Brillas, E. and Casado, J., *Aniline degradation by Electro-Fenton® and peroxi-coagulation processes using a flow reactor for wastewater treatment.* Chemosphere, 2002. **47**(3): p. 241-248.
31. Oturan, M.A., Pimentel, M., Oturan, N., and Sirés, I., *Reaction sequence for the mineralization of the short-chain carboxylic acids usually formed upon cleavage of aromatics during electrochemical Fenton treatment.* Electrochimica Acta, 2008. **54**(2): p. 173-182.
32. Li, L., Zhu, W., Chen, L., Zhang, P., and Chen, Z., *Photocatalytic ozonation of dibutyl phthalate over TiO2 film.* Journal of Photochemistry and photobiology A: Chemistry, 2005. **175**(2-3): p. 172-177.
33. Wang, X., Dou, L., Yang, L., Yu, J., and Ding, B., *Hierarchical structured MnO2@ SiO2 nanofibrous membranes with superb flexibility and enhanced catalytic performance.* Journal of hazardous materials, 2017. **324**: p. 203-212.
34. Xu, P., Drewes, J.E., Bellona, C., Amy, G., Kim, T.U., Adam, M., and Heberer, T., *Rejection of emerging organic micropollutants in nanofiltration–reverse osmosis membrane applications.* Water Environment Research, 2005. **77**(1): p. 40-48.
35. Book, G., *Compendium of chemical terminology.* International Union of Pure and Applied Chemistry, 2014. **528**.
36. Chen, D., Zhang, J., and Chen, J., *Adsorption of methyl tert-butyl ether using granular activated carbon: Equilibrium and kinetic analysis*. International Journal of Environmental Science & Technology, 2010. **7**: p. 235-242.
37. Navarathna, C.M., Bombuwala Dewage, N., Keeton, C., Pennisson, J., Henderson, R., Lashley, B., Zhang, X., Hassan, E.B., Perez, F., and Mohan, D., *Biochar adsorbents with enhanced hydrophobicity for oil spill removal.* ACS applied materials & interfaces, 2020. **12**(8): p. 9248-9260.
38. Yang, L., Wang, Z., Yang, L., Li, X., Zhang, Y., and Lu, C., *Coco peat powder as a source of magnetic sorbent for selective oil–water separation.* Industrial crops and products, 2017. **101**: p. 1-10.
39. Ake, C., Wiles, M., Huebner, H., McDonald, T., Cosgriff, D., Richardson, M., Donnelly, K., and Phillips, T., *Porous organoclay composite for the sorption of polycyclic aromatic hydrocarbons and*

pentachlorophenol from groundwater. Chemosphere, 2003. **51**(9): p. 835-844.

40. Beall, G.W., *The use of organo-clays in water treatment.* Applied clay science, 2003. **24**(1-2): p. 11-20.
41. Sidik, S., Jalil, A., Triwahyono, S., Adam, S., Satar, M., and Hameed, B., *Modified oil palm leaves adsorbent with enhanced hydrophobicity for crude oil removal.* Chemical Engineering Journal, 2012. **203**: p. 9-18.
42. Yang, Z., Wu, X., Han, J., Xu, S., Li, F., Guan, F., and Qiu, Y., *Superhydrophobically modified kapok fiber and powder: Surface characteristic, oil sorption and pore structure.* Industrial Crops and Products, 2024. **209**: p. 117960.
43. Zhou, S., Liu, P., Wang, M., Zhao, H., Yang, J., and Xu, F., *Sustainable, reusable, and superhydrophobic aerogels from microfibrillated cellulose for highly effective oil/water separation.* ACS Sustainable Chemistry & Engineering, 2016. **4**(12): p. 6409-6416.
44. Zhang, Q., Deng, S., Yu, G., and Huang, J., *Removal of perfluorooctane sulfonate from aqueous solution by crosslinked chitosan beads: sorption kinetics and uptake mechanism.* Bioresource technology, 2011. **102**(3): p. 2265-2271.
45. Kalbuadi, D.N., Goenadi, D.H., Santi, L.P., and Nurtjahja, L.R., *The potential use of natural clinoptilolite zeolite for crude oil spill removal from sea water.* Journal of Minerals and Materials Characterization and Engineering, 2019. **7**(06): p. 446.
46. Shavandi, M., Haddadian, Z., Ismail, M.H.S., Abdullah, N., and Abidin, Z., *Removal of residual oils from palm oil mill effluent by adsorption on natural zeolite.* Water, Air, & Soil Pollution, 2012. **223**: p. 4017-4027.
47. Bandura, L., Panek, R., Madej, J., and Franus, W., *Synthesis of zeolite-carbon composites using high-carbon fly ash and their adsorption abilities towards petroleum substances.* Fuel, 2021. **283**: p. 119173.
48. Bouyarmane, H., El Asri, S., Rami, A., Roux, C., Mahly, M., Saoiabi, A., Coradin, T., and Laghzizil, A., *Pyridine and phenol removal using natural and synthetic apatites as low cost sorbents: influence of porosity and surface interactions.* Journal of hazardous materials, 2010. **181**(1-3): p. 736-741.
49. Sun, D., Zhang, X., Wu, Y., and Liu, X., *Adsorption of anionic dyes from aqueous solution on fly ash.* Journal of hazardous materials, 2010. **181**(1-3): p. 335-342.
50. Gupta, V.K., Mohan, D., Sharma, S., and Sharma, M., *Removal of basic dyes (rhodamine B and methylene blue) from aqueous solutions using bagasse fly ash.* Separation Science and Technology, 2000. **35**(13): p. 2097-2113.
51. Wan, W., Zhang, R., Li, W., Liu, H., Lin, Y., Li, L., and Zhou, Y., *Graphene–carbon nanotube aerogel as an ultra-light, compressible and recyclable highly efficient absorbent for oil and dyes.* Environmental Science: Nano, 2016. **3**(1): p. 107-113.
52. Zhan, W., Yu, S., Gao, L., Wang, F., Fu, X., Sui, G., and Yang, X., *Bioinspired assembly of carbon nanotube into graphene aerogel with "cabbagelike" hierarchical porous structure for highly efficient organic pollutants cleanup.* ACS applied materials & interfaces, 2018. **10**(1): p. 1093-1103.
53. Ren, J., Zhou, J., Kong, Y., Jiang, X., and Shen, X., *Development of regular hydrophobic silica aerogel microspheres for efficient oil adsorption.* Langmuir, 2022. **39**(1): p. 478-486.
54. Yu, L., Hao, G., Liang, Q., Zhou, S., Zhang, N., and Jiang, W., *Facile preparation and characterization of modified magnetic silica nanocomposite particles for oil absorption.* Applied Surface Science, 2015. **357**: p. 2297-2305.
55. Cho, Y.-S., Sung, S., Woo, S.H., and Kim, Y.S., *Optimization of oil adsorption capacity by aerogel*

powder synthesized using emulsion droplets as micro-reactors in ambient conditions from sodium silicate as precursor. Korean Journal of Metals and Materials, 2021. **59**(2): p. 99-112.

56. Sun, T., Hao, S., Fan, R., Qin, M., Chen, W., Wang, P., and Yang, Y., *Hydrophobicity-adjustable mof constructs superhydrophobic mof-rgo aerogel for efficient oil–water separation.* ACS Applied Materials & Interfaces, 2020. **12**(50): p. 56435-56444.
57. Xue, J., Xu, M., Gao, J., Zong, Y., Wang, M., and Ma, S., *Multifunctional porphyrinic Zr-MOF composite membrane for high-performance oil-in-water separation and organic dye adsorption/photocatalysis*. Colloids and Surfaces A: Physicochemical and Engineering Aspects, 2021. **628**: p. 127288.
58. Su, Y., Li, Z., Zhou, H., Kang, S., Zhang, Y., Yu, C., and Wang, G., *Ni/carbon aerogels derived from water induced self-assembly of Ni-MOF for adsorption and catalytic conversion of oily wastewater.* Chemical Engineering Journal, 2020. **402**: p. 126205.
59. Ruidas, S., Das, A., Kumar, S., Dalapati, S., Manna, U., and Bhaumik, A., *Non-Fluorinated and Robust Superhydrophobic Modification on Covalent Organic Framework for Crude-Oil-in-Water Emulsion Separation.* Angewandte Chemie, 2022. **134**(41): p. e202210507.
60. Karmelich, C., Wan, Z., Tian, W., Crooke, E., Qi, X., Carroll, A., Konstas, K., and Wood, C., *Advancing hyper-crosslinked materials with high efficiency and reusability for oil spill response.* Scientific Reports, 2023. **13**(1): p. 9779.
61. Xue, T., Wang, M., Man, J., Yang, Y., Miao, H., and Li, X., *Construction and Regulation of a Superhydrophobic Sponge via In Situ Anchoring of a Hyper-Cross-Linked Polymer for Efficient Oil/Water Separation.* ACS Applied Polymer Materials, 2024. **6**(7): p. 3864-3874.
62. Lin, J., Xia, X., Liu, Y., Luan, Z., Chen, Y., Ma, K., Geng, B., and Li, H., *Fabrication of hierarchical porous fluoro-PolyHIPE materials with ultra-high specific surface area via hypercrosslinking knitting technique.* Journal of Applied Polymer Science, 2022. **139**(38): p. e52914.
63. Sheng, Q., Tian, W., and Wood, C.D., *Hyper-cross-linked polymer-decorated surfaces with ultrahigh efficiency for oil/water emulsion separation and recovery.* ACS Applied Materials & Interfaces, 2021. **13**(33): p. 39925-39933.
64. Pan, B., Zhang, X., Jiang, Z., Li, Z., Zhang, Q., and Chen, J., *Polymer and polymer-based nanocomposite adsorbents for water treatment.* Polymeric Materials for Clean Water, 2019: p. 93-119.
65. Yang, Z., Wu, G., Li, Q., Ai, H., Yao, X., and Ji, H., *Removal of various pollutants from wastewaters using an efficient and degradable hypercrosslinked polymer.* Separation Science and Technology, 2021. **56**(5): p. 860-869.
66. Waheed, A., Baig, N., Ullah, N., and Falath, W., *Removal of hazardous dyes, toxic metal ions and organic pollutants from wastewater by using porous hyper-cross-linked polymeric materials: A review of recent advances*. Journal of Environmental Management, 2021. **287**: p. 112360.
67. Zhang, A., Chen, M., Du, C., Guo, H., Bai, H., and Li, L., *Poly (dimethylsiloxane) oil absorbent with a three-dimensionally interconnected porous structure and swellable skeleton.* ACS applied materials & interfaces, 2013. **5**(20): p. 10201-10206.
68. Churipard, S.R., Kanakikodi, K.S., Rambhia, D.A., Raju, C.S.K., Halgeri, A., Choudary, N.V., Ganesh, G.S., Ravishankar, R., and Maradur, S.P., *Porous polydivinylbenzene (PDVB) as an efficient adsorbent for hydrocarbons: Effect of porogens on adsorption capacity.* Chemical Engineering Journal, 2020. **380**: p. 122481.
69. Srivastava, S., Tyagi, R., Pal, N., and Mohan, D., *Process development for removal of substituted*

phenol by carbonaceous adsorbent obtained from fertilizer waste. Journal of Environmental Engineering, 1997. **123**(9): p. 842-851.

70. Karcher, S., Kornmüller, A., and Jekel, M., *Anion exchange resins for removal of reactive dyes from textile wastewaters.* Water research, 2002. **36**(19): p. 4717-4724.
71. Rouquerol, J., Avnir, D., Fairbridge, C.W., Everett, D.H., Haynes, J., Pernicone, N., Ramsay, J.D., Sing, K.S.W., and Unger, K.K., *Recommendations for the characterization of porous solids (Technical Report).* Pure and applied chemistry, 1994. **66**(8): p. 1739-1758.
72. Thommes, M., Kaneko, K., Neimark, A.V., Olivier, J.P., Rodriguez-Reinoso, F., Rouquerol, J., and Sing, K.S., *Physisorption of gases, with special reference to the evaluation of surface area and pore size distribution (IUPAC Technical Report).* Pure and applied chemistry, 2015. **87**(9-10): p. 1051-1069.
73. Mohamed, M.G., EL-Mahdy, A.F., Kotp, M.G., and Kuo, S.-W., *Advances in porous organic polymers: Syntheses, structures, and diverse applications.* Materials Advances, 2022. **3**(2): p. 707-733.
74. Huang, J. and Turner, S.R., *Hypercrosslinked polymers: a review.* Polymer Reviews, 2018. **58**(1): p. 1-41.
75. Raza, S., Nazeer, S., Abid, A., and Kanwal, A., *Recent research progress in the synthesis, characterization and applications of hyper cross-linked polymer.* Journal of Polymer Research, 2023. **30**(11): p. 415.
76. Davankov, V. and Tsyurupa, M., *Structure and properties of hypercrosslinked polystyrene—the first representative of a new class of polymer networks.* Reactive Polymers, 1990. **13**(1-2): p. 27-42.
77. Pan, B., Du, W., Zhang, W., Zhang, X., Zhang, Q., Pan, B., Lv, L., Zhang, Q., and Chen, J., *Improved adsorption of 4-nitrophenol onto a novel hyper-cross-linked polymer.* Environmental science & technology, 2007. **41**(14): p. 5057-5062.
78. Zeng, X., Fan, Y., Wu, G., Wang, C., and Shi, R., *Enhanced adsorption of phenol from water by a novel polar post-crosslinked polymeric adsorbent.* Journal of hazardous materials, 2009. **169**(1-3): p. 1022-1028.
79. Zhang, N., Qi, Y., Zhang, Y., Luo, J., Cui, P., and Jiang, W., *A review on oil/water mixture separation material.* Industrial & Engineering Chemistry Research, 2020. **59**(33): p. 14546-14568.
80. Liu, T., Zhao, G., Zhang, W., Chi, H., Hou, C., and Sun, Y., *The preparation of superhydrophobic graphene/melamine composite sponge applied in treatment of oil pollution.* Journal of Porous materials, 2015. **22**: p. 1573-1580.
81. Plummer, L.N. and Busenberg, E., *Chlorofluorocarbons*, in *Environmental tracers in subsurface hydrology*. 2000, Springer. p. 441-478.
82. Höhener, P., Werner, D., Balsiger, C., and Pasteris, G., *Worldwide occurrence and fate of chlorofluorocarbons in groundwater.* 2003.
83. Luo, Y., Yang, Z., Suo, X., Chen, H., Wang, T., Wang, Z., Liu, Y., Lyu, Y., Popovs, I., and Dai, S., *Robust perfluorinated porous organic networks: Succinct synthetic strategy and application in chlorofluorocarbons adsorption.* Nano Research, 2021. **14**: p. 3282-3287.
84. Wood, C.D., Tan, B., Trewin, A., Niu, H., Bradshaw, D., Rosseinsky, M.J., Khimyak, Y.Z., Campbell, N.L., Kirk, R., and Stöckel, E., *Hydrogen storage in microporous hypercrosslinked organic polymer networks.* Chemistry of materials, 2007. **19**(8): p. 2034-2048.
85. Martín, C.F., Stöckel, E., Clowes, R., Adams, D.J., Cooper, A.I., Pis, J.J., Rubiera, F., and Pevida, C., *Hypercrosslinked organic polymer networks as potential adsorbents for pre-combustion CO 2 capture.* Journal of Materials Chemistry, 2011. **21**(14): p. 5475-5483.

86. Schweng, P., Mayer, F., Galehdari, D., Weiland, K., and Woodward, R.T., *A Robust and Low-Cost Sulfonated Hypercrosslinked Polymer for Atmospheric Water Harvesting.* Small, 2023.
87. Hubert, O., Todorovic, N., González, L.M.R., Costagliola, E., Blocher, A., Mautner, A., Woodward, R.T., and Bismarck, A., *Sulfonated hypercrosslinked polymer enhanced structural composite supercapacitors.* Composites Science and Technology, 2023. **242**: p. 110152.
88. Saha, B.K., Veluthaparambath, R.V., and Krishna G, V., *Halogen··· halogen interactions: nature, directionality and applications.* Chemistry–An Asian Journal, 2023. **18**(8): p. e202300067.
89. Nesterenko, E., Skornyakov, V., Nesterenko, P., and Ivanov, A., *Use of linear solvation energy relationships for characterization of hypercrosslinked polystyrene stationary phases.* Moscow University Chemistry Bulletin, 2008. **63**(1): p. 23-29.
90. Neimark, A.V., Lin, Y., Ravikovitch, P.I., and Thommes, M., *Quenched solid density functional theory and pore size analysis of micro-mesoporous carbons.* Carbon, 2009. **47**(7): p. 1617-1628.
91. Sarkar, A. and Mahapatra, S., *Novel hydrophobic vaterite particles for oil removal and recovery.* Journal of Materials Chemistry A, 2014. **2**(11): p. 3808-3818.
92. Ramasamy, R., *FTIR and FT-RAMAN spectral investigation of fluorobenzene.* Int. J. Phys. Appl, 2014. **6**(1): p. 1-6.
93. Knauber, T., Arikan, F., Röschenthaler, G.V., and Gooßen, L.J., *Copper-Catalyzed Trifluoromethylation of Aryl Iodides with Potassium (Trifluoromethyl) trimethoxyborate.* Chemistry–A European Journal, 2011. **17**(9): p. 2689-2697.
94. Kildahl, N.K., *Bond energy data summarized.* Journal of chemical education, 1995. **72**(5): p. 423.
95. Vincent, B. *The International XPS Database*. 2021-2024 [cited September 25, 2024; Available from: https://xpsdatabase.net/.
96. Reddy, P.M., Chang, C.-J., Chen, J.-K., Wu, M.-T., and Wang, C.-F., *Robust polymer grafted Fe3O4 nanospheres for benign removal of oil from water.* Applied Surface Science, 2016. **368**: p. 27-35.
97. Shao, M., Junejo, S.A., Zhang, B., and Huang, Q., *Effects of explosion puffing on the native structural organization and oil adsorption properties of starch.* Carbohydrate Polymers, 2024. **324**: p. 121518.
98. Yu, Y., Guo, D., and Fang, J., *Synthesis of silica aerogel microspheres by a two-step acid–base sol–gel reaction with emulsification technique.* Journal of Porous Materials, 2015. **22**: p. 621-628.